INTERNATIONAL JOURNAL FOR NUMERICAL METHODS IN FLUIDS
Int. J. Numer. Meth. Fluids 2010; **62**:963–993
Published online 20 April 2009 in Wiley InterScience (www.interscience.wiley.com). DOI: 10.1002/fld.2051

Numerical simulation of bubble and droplet deformation by a level set approach with surface tension in three dimensions

Roberto Croce, Michael Griebel and Marc Alexander Schweitzer*, †

Institut für Numerische Simulation, Universität Bonn, Wegelerstr. 6, D-53115 Bonn, Germany

SUMMARY

In this paper we present a three-dimensional Navier–Stokes solver for incompressible two-phase flow problems with surface tension and apply the proposed scheme to the simulation of bubble and droplet deformation. One of the main concerns of this study is the impact of surface tension and its discretization on the overall convergence behavior and conservation properties.

Our approach employs a standard finite difference/finite volume discretization on uniform Cartesian staggered grids and uses Chorin's projection approach. The free surface between the two fluid phases is tracked with a level set (LS) technique. Here, the interface conditions are implicitly incorporated into the momentum equations by the continuum surface force method. Surface tension is evaluated using a smoothed delta function and a third-order interpolation. The problem of mass conservation for the two phases is treated by a reinitialization of the LS function employing a regularized signum function and a global fixed point iteration. All convective terms are discretized by a WENO scheme of fifth order. Altogether, our approach exhibits a second-order convergence away from the free surface. The discretization of surface tension requires a smoothing scheme near the free surface, which leads to a first-order convergence in the smoothing region.

We discuss the details of the proposed numerical scheme and present the results of several numerical experiments concerning mass conservation, convergence of curvature, and the application of our solver to the simulation of two rising bubble problems, one with small and one with large jumps in material parameters, and the simulation of a droplet deformation due to a shear flow in three space dimensions. Furthermore, we compare our three-dimensional results with those of quasi-two-dimensional and two-dimensional simulations. This comparison clearly shows the need for full three-dimensional simulations of droplet and bubble deformation to capture the correct physical behavior. Copyright © 2009 John Wiley & Sons, Ltd.

Received 22 March 2008; Revised 2 December 2008; Accepted 7 February 2009

KEY WORDS: incompressible two-phase flow; surface tension; capillarity; continuum surface force method; level set method; droplet deformation

*Correspondence to: Marc Alexander Schweitzer, Institut für Numerische Simulation, Universität Bonn, Wegelerstr. 6, D-53115 Bonn, Germany.
†E-mail: schweitzer@ins.uni-bonn.de

Contract/grant sponsor: Deutsche Forschungsgemeinschaft

1. INTRODUCTION

Many problems in fluid flow applications require the consideration of two incompressible immiscible fluids and, consequently, the treatment of the free surface between these two phases. Important examples are the deformation of liquid–gas interfaces by aerodynamical forces as it occurs in spray injection and atomization in liquid propulsion [1]. A reference problem in dispersion science, emulsification, and mixing is the deformation of a liquid droplet due to a surrounding shear flow. In such mesoscopic flow problems, when the characteristic length scale of the flow is relatively small, surface tension effects cannot be neglected as in (most) macroscopic flows. The forces due to surface tension play an essential role for the overall dynamics and determine the deformation behavior of the interface. This class of applications pose a number of challenges to numerical methods. The most substantial is the representation of the moving interface that separates the two different fluid phases and their associated material properties such as density and viscosity, and the appropriate treatment of surface tension effects.

Classical approaches to the tracking of moving interfaces are the Marker and Cell (MAC) schemes [2–10] where the two fluid phases are explicitly represented by massless marker particles and the interface needs to be reconstructed from the distribution of the marker particles. The accurate representation of the moving interface, however, requires a large number of marker particles and thereby a substantial computational effort. In the volume of fluid (VOF) technique [11–18] the characteristic functions of the two fluid domains are directly approximated on the underlying mesh by a piecewise constant function. Hence, the reconstruction of a smooth interface, i.e. the accurate computation of curvature which is necessary for simulations involving surface tension effects, is not straightforward in the VOF and requires sophisticated interpolation schemes [19, 20]. This drawback is overcome in the level set (LS) approach [21–23] where the characteristic functions of the two fluid phases are approximated by the sign of a smooth scalar function, so that the interface is given by the zero LS of this smooth function. Owing to this smooth approximation the computation of curvature is straightforward.

The movement of the interface, however, may lead to a substantial distortion of the LS function over time; i.e. its gradient may become very large or very small near the interface that can adversely affect the stable evaluation of surface tension terms. To overcome this issue, a so-called reinitialization step must be performed. Here, the current LS function is replaced by a smoother, less distorted function, which has (approximately) the same zero LS. Yet, the reinitalization may compromise the mass conservation properties of the numerical scheme. A widely used and very successful approach is the reinitialization by a signed distance function, see e.g. [24–28]. Such a simple reinitialization technique, however, introduces numerical diffusion to the solution, which leads to a deterioration of the volume conservation, i.e. mass conservation in incompressible flow. To this end, several modified reinitialization methods have been developed to improve the mass conservation [29–32]. The interplay between these techniques and the convergence behavior of surface tension terms within a full two-phase flow solver is not completely understood.

The second major challenge encountered in the simulation of multi-phase flows on the mesoscale is the numerical treatment of surface tension effects that cannot be neglected. One approach to the treatment of surface tension is by variational techniques based on the Laplace–Beltrami operator on the free surface [33–37]. Another widely used approach is the continuum surface force (CSF) scheme [10, 38]. Here, surface tension, i.e. the respective interface condition, is modeled as a body force acting on grid cells that contain the interface. This approach was introduced in the context of VOF and MAC methods, but it is directly applicable to the LS approach as well [28]. Even though

DOI: 10.1002/fld

the CSF approach is reported to be quite robust, to our knowledge, the convergence behavior of surface tension terms approximated by the CSF in conjunction with a level set method (LSM) within a full two-phase flow solver is also not completely understood.

In this paper we present a three-dimensional incompressible Navier–Stokes solver for two-phase flow problems based on Chorin's projection approach on staggered Cartesian grids, the LS technique, and the CSF scheme for the treatment of surface tension effects. To cope with the issue of mass conservation, we employ an improved reinitialization scheme essentially due to [32] in conjunction with a fifth-order WENO scheme and an additional fixed point iteration to enforce the conservation of the global mass explicitly. We apply our solver to several reference problems to validate the presented numerical scheme and to study the effect of, e.g. the reinitialization of the LS function on the overall convergence behavior and conservation properties. For instance, we study the test problem of a rising air bubble in water in two and three dimensions. Our two-dimensional results compare very well with references from the literature [39, 40] for small times and we attain more reliable results for large simulation times since we not only employ a higher-order transport scheme for the LS function, but also attain mass conservation. A comparison of the two-dimensional results with the computed three-dimensional results shows distinct differences, which clearly indicates the need for three-dimensional simulations in the study of bubble and droplet deformation in general. Furthermore, we consider the deformation of a droplet in three dimensions due to a shear flow.

The remainder of this paper is organized as follows. The employed mathematical model is presented in Section 2. Here, we implement the coupling of the Navier–Stokes equations for two flow phases by the classical interface conditions which incorporate surface tension. To this end, we discuss the CSF method in the context of the LSM. The discretization of the coupled model is presented in some detail in Section 3. The Navier–Stokes equations as well as the transport equation for the LS function are discretized in time using an Adams–Bashford method of second order, whereas the reinitialization of the LS function is discretized in time using an explicit third-order Runge–Kutta scheme. The discretization in space employs a standard finite difference/finite volume approach on a staggered uniform grid. Furthermore, we use a signed distance function in the LS representation of the free surface, a fifth-order WENO scheme for all convective terms, a higher-order interpolation scheme for the LS function and an improved reinitialization scheme including a global fixed point iteration to enforce mass conservation. In Section 4 we present the results of several numerical experiments for model problems concerning mass conservation, convergence of curvature, and convergence of the complete two-phase flow scheme. We study for instance rising air bubble in water in three dimensions and its two-dimensional analogue and compare our results to two-dimensional simulations from the literature. Here it turns out that the results in three dimensions differ quite substantially from those computed in two dimensions which clearly indicate the need for three-dimensional simulation of bubble and droplet dynamics. Finally, we consider the deformation of a liquid droplet due to a surrounding shear flow. We conclude with some remarks in Section 5.

2. MATHEMATICAL MODEL

The behavior of two immiscible incompressible fluids is governed by the incompressible Navier–Stokes equations defined on an open set $\Omega = \Omega_1 \cup \Omega_2 \cup \Gamma_f \subset \mathbb{R}^3$ with Lipschitz boundary $\Gamma := \partial\Omega$. Here, Ω_1 and Ω_2 denote the subdomains associated with the two different fluid phases, respectively.

DOI: 10.1002/fld

The free interface between the two fluid phases is denoted by $\Gamma_f := \partial\Omega_1 \cap \partial\Omega_2$. The two fluid domains Ω_1 and Ω_2 and the free interface Γ_f depend on time. The temporal evolution of each of the fluids is described by the classical Navier–Stokes equations in its respective subdomain Ω_i for $t \in [0, T]$; i.e. we have

$$\begin{aligned} \rho_i \frac{D\mathbf{u}_i}{Dt} &= -\nabla p_i + \nabla \cdot (\mu_i \mathbf{S}_i) + \rho_i \mathbf{g} \quad \text{in } \Omega_i \\ \nabla \cdot \mathbf{u}_i &= 0 \quad \text{in } \Omega_i \\ \mathbf{u}_i|_\Gamma &= 0 \quad \text{in } [0, T] \\ \mathbf{u}_i|_{t=0} &= u_{0_i} \quad \text{in } \Omega_i \end{aligned} \tag{1}$$

where $i \in \{1, 2\}$ indicates the considered fluid phase. Furthermore, $\mathbf{u}_i$ denotes the velocity field, p_i the pressure, μ_i the dynamic viscosity, ρ_i the density, and $\mathbf{g}$ the volume force. The viscous stress tensor is given by $\mathbf{S}_i := \nabla \mathbf{u}_i + \{\nabla \mathbf{u}_i\}^{\mathrm{T}}$ and the material derivative by $D(\mathbf{u}_i)/Dt := \partial_t(\mathbf{u}_i) + (\mathbf{u}_i \cdot \nabla)\mathbf{u}_i$. The values of μ_i and ρ_i in each phase are assumed to be constant. However, the system (1) is *not* complete without some additional conditions imposed on the free interface Γ_f.

The basic assumption in continuum mechanics for the free boundary Γ_f is that it can be regarded as a sharp interface; i.e. the interface is a two-dimensional surface, which separates the two flow regions. For immiscible fluids this can be justified by dimension analysis, see [41] for a detailed discussion. Hence, our two-phase flow model contains a jump in density and a jump in viscosity across the free surface. A consequence of this assumption is that the interface possesses no mass. Consequently, the net stress vanishes along the interface. Furthermore, the velocity must be continuous across the free surface, i.e. $\mathbf{u}_1 = \mathbf{u}_2$ on Γ_f. For a more detailed discussion see [41]. The surface tension boundary conditions at the interface Γ_f between the two fluid phases are given by

$$(\mathbf{T}_1 - \mathbf{T}_2) \cdot \mathbf{n} = \sigma\kappa\mathbf{n}, \quad (\mathbf{T}_1 - \mathbf{T}_2) \cdot \mathbf{t} = \frac{\partial\sigma}{\partial\mathbf{t}} \quad \text{and} \quad (\mathbf{T}_1 - \mathbf{T}_2) \cdot \mathbf{s} = \frac{\partial\sigma}{\partial\mathbf{s}}$$

where $\mathbf{T}_i := -p_i\mathbf{I} + \mu_i\mathbf{S}_i$ denotes the stress tensor, σ is the surface tension coefficient determined by the physical properties of the considered fluids, and $\mathbf{n} := \mathbf{n}_1 = -\mathbf{n}_2$ denotes the surface normal on Γ_f, i.e. the outer normal on $\partial\Omega_1$. The local curvature κ is given by

$$\kappa = \frac{1}{R_t} + \frac{1}{R_s} \tag{2}$$

with the radii R_t and R_s of curvature along the coordinates t and s as shown in Figure 1. We assume that the material properties μ_i and ρ_i are constant in each Ω_i and that the surface tension coefficient σ is constant throughout the *whole* domain Ω. Therefore, the conditions on the interface Γ_f reduce to

$$\mathbf{u}_1 = \mathbf{u}_2 \tag{3}$$

$$(\mathbf{T}_1 - \mathbf{T}_2) \cdot \mathbf{n} = \sigma\kappa\mathbf{n} \tag{4}$$

$$(\mathbf{T}_1 - \mathbf{T}_2) \cdot \mathbf{t} = 0 \tag{5}$$

$$(\mathbf{T}_1 - \mathbf{T}_2) \cdot \mathbf{s} = 0 \tag{6}$$

DOI: 10.1002/fld

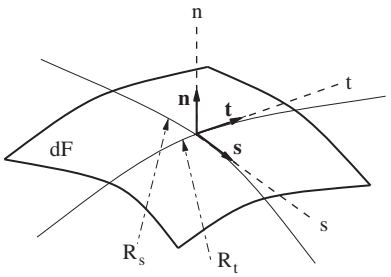

Figure 1. Curvature for surface tension computation.

Throughout this paper, we consider surface tension forces in normal direction only. Hence, we complete the Navier–Stokes equations (1) in each of the subdomains Ω_i with the interface conditions (3) and (4), whereas the tangential conditions (5) and (6) are not explicitly enforced. Altogether, the complete model for two-phase flow problems including surface tension considered in this paper is given by

$$\begin{aligned}
\rho_i \frac{D\mathbf{u}_i}{Dt} &= -\nabla p_i + \nabla\cdot(\mu_i \mathbf{S}_i) + \rho_i \mathbf{g} \quad \text{in } \Omega_i \\
\nabla\cdot\mathbf{u}_i &= 0 \quad \text{in } \Omega_i \\
\mathbf{u}_i|_\Gamma &= 0 \quad \text{in } [0,T] \\
\mathbf{u}_i|_{t=0} &= u_{0_i} \quad \text{in } \Omega_i \\
\mathbf{u}_1 &= \mathbf{u}_2 \quad \text{on } \Gamma_f \\
(\mathbf{T}_1 - \mathbf{T}_2)\cdot\mathbf{n} &= \sigma\kappa\mathbf{n} \quad \text{on } \Gamma_f
\end{aligned} \tag{7}$$

for $i \in \{1,2\}$.

2.1. Formulation of surface tension within the momentum equations

To couple the two-phase-flow Navier–Stokes equations (1) with the free surface boundary conditions (4), we start from the integral form of (1)

$$\int_{\Omega_i} \rho_i \frac{D(\mathbf{u}_i)}{Dt}\,\mathrm{d}\mathbf{x} = \int_{\partial\Omega_i} \mathbf{T}_i\cdot\mathbf{n}\,\mathrm{d}F + \int_{\Omega_i} \rho_i \mathbf{g}\,\mathrm{d}\mathbf{x} \tag{8}$$

for $i \in \{1,2\}$. Summation of both momentum equations (8) yields

$$\rho_1 \int_{\Omega_1} \frac{D\mathbf{u}}{Dt}\,\mathrm{d}\mathbf{x} + \rho_2 \int_{\Omega_2} \frac{D\mathbf{u}}{Dt}\,\mathrm{d}\mathbf{x} = \int_{\partial\Omega} \mathbf{T}\cdot\mathbf{n}\,\mathrm{d}F - \int_{\Gamma_f} [\mathbf{T}]\cdot\mathbf{n}\,\mathrm{d}F + \rho_1 \int_{\Omega_1} \mathbf{g}\,\mathrm{d}\mathbf{x} + \rho_2 \int_{\Omega_2} \mathbf{g}\,\mathrm{d}\mathbf{x} \tag{9}$$

where $\mathbf{T} := \mathbf{T}_1\chi_{\Omega_1} + \mathbf{T}_2\chi_{\Omega_2}$ is defined with the help of the characteristic functions χ_{Ω_1} and χ_{Ω_2} associated with the fluid domains Ω_1 and Ω_2, respectively. Furthermore, $[\mathbf{T}]$ denotes the jump in

DOI: 10.1002/fld

the stress tensor T, i.e. $[\mathbf{T}]=\mathbf{T}_1-\mathbf{T}_2$ at the interface Γ_f. With (4) and the Gauß Theorem, we obtain

$$\int_{\partial\Omega}\mathbf{T}\cdot\mathbf{n}\,\mathrm{d}F=\int_{\Omega}\nabla\cdot\mathbf{T}\,\mathrm{d}\mathbf{x} \tag{10}$$

Since $\mathbf{T}$ is discontinuous at the free surface due to the jump in the viscosity, relation (10) is to be understood in the sense of distributions.

With (3), the velocity-field $\mathbf{u}=\mathbf{u}_1\chi_{\Omega_1}+\mathbf{u}_2\chi_{\Omega_2}$ for viscous fluids is continuous on Ω and we can write

$$\rho_1\int_{\Omega_1}\frac{D\mathbf{u}}{Dt}\,\mathrm{d}\mathbf{x}+\rho_2\int_{\Omega_2}\frac{D\mathbf{u}}{Dt}\,\mathrm{d}\mathbf{x}=\int_{\Omega}\rho\frac{D\mathbf{u}}{Dt}\,\mathrm{d}\mathbf{x} \tag{11}$$

Using (4) and substituting (10) and (11) into (9) and obtain the integral formulation of incompressible two-phase flow with surface tension

$$\int_{\Omega}\rho\frac{D\mathbf{u}}{Dt}\,\mathrm{d}\mathbf{x}=\int_{\Omega}\nabla\cdot\mathbf{T}\,\mathrm{d}\mathbf{x}-\int_{\Gamma_f}\sigma\kappa\mathbf{n}\,\mathrm{d}F+\int_{\Omega}\rho\mathbf{g}\,\mathrm{d}\mathbf{x} \tag{12}$$

The advantage of (12) is that the boundary condition for surface tension is implicitly contained in the momentum equation. However, it is still formulated as a free boundary integral. For the discretization we convert this free boundary integral to a volume integral via the CSF approach [10, 38]. Then, we can easily couple the momentum equation with a LS formulation which does not require an explicit reconstruction of the free surface, compare also [42, 43]. Note that this is in contrast to most VOF methods where a reconstruction of Γ_f is often required even with a CSF formulation.

2.2. The CSF-approach in the LSM

The CSF model was first proposed by Brackbill *et al.* [38] for VOF methods and by Unverdi and Tryggvason [10] for MAC methods. We now give a short description of the CSF approach in the framework of the LSM, see [28] for details.

The aim is to provide a unified formulation of (7) on the compete domain Ω; i.e. we will eliminate the explicit interface conditions in (7). To this end, we start from the two-phase flow equations in integral form (12). There, surface tension is included as a source term on the right-hand side. This free boundary integral needs to be converted into a volume integral to obtain the associated differential formulation of the Navier–Stokes equations including surface tension by passing to the limit of infinitesimally small volumes.

To this end, we construct a function ϕ such that the interface between the two different fluids is the zero LS of ϕ (compare Figure 2). The interface is then given by

$$\Gamma_f(t)=\{\mathbf{x}:\phi(\mathbf{x},t)=0\}$$

for all times $t\in[0,T]$. Note that there are arbitrarily many ways to define the LS function ϕ away from the free surface. Here, we choose ϕ as a signed distance function such that

$$\phi(\mathbf{x},t)\begin{cases}<0 & \text{if } \mathbf{x}\in\Omega_1\\ =0 & \text{if } \mathbf{x}\in\Gamma_f\\ >0 & \text{if } \mathbf{x}\in\Omega_2\end{cases} \tag{13}$$

DOI: 10.1002/fld

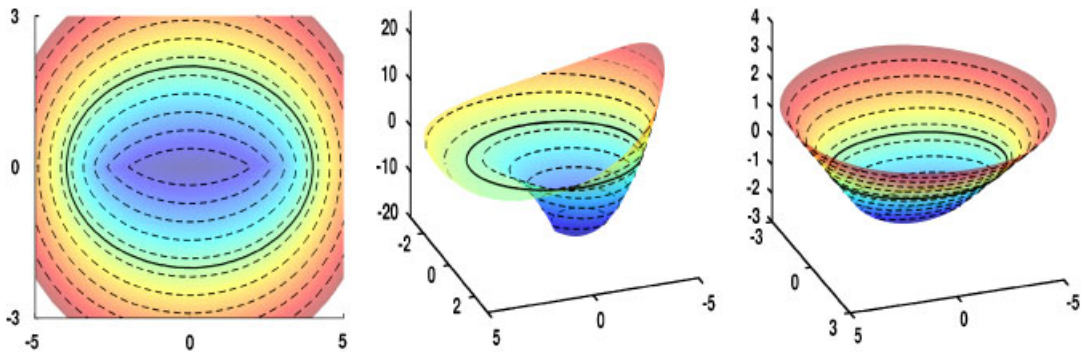

Figure 2. Elliptical zero-level set (left; bold line, top view), surface plot of a general level set function with the same elliptical zero-level set (center), and a surface plot of a respective signed distance level set function (right).

hold and the Eikonal equation $|\nabla\phi|=1$ is fulfilled (compare Figure 2). With the help of this LS function ϕ we can now easily define the density ρ and the viscosity μ on the whole domain, i.e. of both fluid phases. To this end, we set

$$\rho(\phi):=\rho_2+(\rho_1-\rho_2)H(\phi) \quad \text{and} \quad \mu(\phi):=\mu_2+(\mu_1-\mu_2)H(\phi) \tag{14}$$

where $H(\phi)$ denotes the Heaviside function, which is defined as

$$H(\phi):=\begin{cases} 0 & \text{if } \phi<0 \\ \frac{1}{2} & \text{if } \phi=0 \\ 1 & \text{if } \phi>0 \end{cases}$$

Note that there are a number of variations in the definition of the mixture viscosity [44, 45] at the interface which yield very similar results for small density and viscosity ratios only. However, the so-called serial average of (14) employed in this study is the most common approach [45].

Now, with these ϕ-dependent material parameters, Equation (12) can be expressed as

$$\int_\Omega \rho(\phi)\frac{D\mathbf{u}}{Dt}\,\mathrm{d}\mathbf{x}=\int_\Omega \nabla\cdot\mathbf{T}\,\mathrm{d}\mathbf{x}-\int_{\Gamma_f}\sigma\kappa\mathbf{n}\,\mathrm{d}F+\int_\Omega \rho(\phi)\mathbf{g}\,\mathrm{d}\mathbf{x} \tag{15}$$

Following Chang *et al.* [46] we now rewrite the free boundary integral as a volume integral with the help of a Dirac δ-functional. Since $\mathbf{n}=\nabla\phi/|\nabla\phi|$ and $|\nabla\phi|=1$, this results in the identity

$$\int_{\Gamma_f}\sigma\kappa\mathbf{n}\,\mathrm{d}F=\int_\Omega \sigma\kappa(\phi(\mathbf{x}))\delta(\phi(\mathbf{x}))\nabla\phi(\mathbf{x})\,\mathrm{d}\mathbf{x} \tag{16}$$

where δ denotes the one-dimensional Dirac δ-functional, i.e. $\int_{\mathbb{R}} f(x)\delta(x)\,\mathrm{d}x=f(0)$ for $f:\mathbb{R}\to\mathbb{R}$, such that $\int_{\mathbb{R}^3}\delta(\phi(\mathbf{x}))\,\mathrm{d}\mathbf{x}=\int_{\Gamma_f}1\,\mathrm{d}s$. We substitute (16) into (15) and obtain

$$\int_\Omega\left(\rho(\phi)\frac{D\mathbf{u}}{Dt}-\nabla\cdot\mathbf{T}+\sigma\kappa(\phi)\delta(\phi)\nabla\phi-\rho(\phi)\mathbf{g}\right)\mathrm{d}\mathbf{x}=0$$

DOI: 10.1002/fld

which now only involves a volume integral. Since this relation holds for any arbitrary volume Ω, we obtain the associated differential equation

$$\rho(\phi)\frac{D\mathbf{u}}{Dt} - \nabla\cdot\mathbf{T} + \sigma\kappa(\phi)\delta(\phi)\nabla\phi - \rho(\phi)\mathbf{g} = 0$$

With the definition of the stress tensor $\mathbf{T} = -p\mathbf{I} + \mu(\phi)\mathbf{S}$, this yields the equation

$$\rho(\phi)\frac{D\mathbf{u}}{Dt} + \nabla p = \nabla\cdot(\mu(\phi)\mathbf{S}) - \sigma\kappa(\phi)\delta(\phi)\nabla\phi + \rho(\phi)\mathbf{g} \tag{17}$$

In addition to (17) we need to take into account the continuity equation

$$\nabla\cdot\mathbf{u} = 0 \tag{18}$$

and the time dependence of the free surface Γ_f. This time-dependent movement is modeled by a simple advection of the interface due to the underlying flow. Hence, we complement (17) and (18) by the simple transport equation

$$\partial_t\phi + \mathbf{u}\cdot\nabla\phi = 0 \tag{19}$$

for the LS function with initial value $\phi_0(\mathbf{x}) = \phi(\mathbf{x}, 0)$.

3. NUMERICAL METHOD

In this section we present our overall numerical scheme for the treatment of the two-phase flow equations with surface tension in three space dimensions as given by (17), (18), and (19). The scheme is based on the well-known projection method. It employs a semi-implicit time-stepping scheme and a finite difference discretization in space on a staggered grid which is also used for the approximation of the LS function. We begin with a short review of the classical projection method before we cover the details of the incorporation of the LSM into the projection scheme. Here, we need to be concerned with three major issues: the movement of the interface and the conservation properties of the overall scheme, the discontinuity of the material properties at the interface, and the accurate approximation of the surface tension.

The movement of the free interface is modeled via the transport equation (19) for the LS function ϕ. Here, we have to deal with the problem of volume and mass conservation of the two different fluid phases. Hence, we employ a fifth-order WENO scheme for the evaluation of all convective terms and reinitialize the LS function ϕ in every time step to maintain the signed distance property of ϕ over time. Furthermore, we use an additional fixed point iteration to enforce the conservation of the global mass explicitly. Note that the discontinuity of the density and viscosity at the interface may lead to spurious oscillations and instabilities; therefore, we need to be concerned with the development of an appropriate smoothing scheme for the material properties. Moreover, it is essential to employ a higher-order interpolation scheme for the LS function to obtain an accurate approximation of the surface tension, i.e. of the curvature. In the following we cover these issues in some more detail.

3.1. Time discretization and projection method

A widely used and very successful scheme for the solution of the incompressible Navier–Stokes equations is the so-called projection method due to Chorin [47]. Here, the starting point is the

DOI: 10.1002/fld

consideration of the time-discrete Navier–Stokes equations using a forward Euler scheme; i.e. we compute the solution $\mathbf{u}^{n+1}$ at time t_{n+1} from the solution $\mathbf{u}^n$ of the previous time step. To obtain the solution of (17) under the constraint (18) in a single Euler step, we employ a two step approach. First, we compute an intermediate velocity field $\mathbf{u}^*$ via an explicit transport, which may not yield $\mathbf{u}^*$ to be divergence free. Then, in a second step, we compute a correction ∇p^{n+1} of the intermediate velocity field $\mathbf{u}^*$ by the pressure Poisson equation which leads to a divergence-free velocity field $\mathbf{u}^{n+1}$; i.e. we treat the pressure (and the LS function) implicitly.

By an Euler time discretization of (17) we obtain the intermediate velocity field $\mathbf{u}^*$ as

$$\frac{\mathbf{u}^*-\mathbf{u}^n}{\delta t}=-(\mathbf{u}^n\cdot\nabla)\mathbf{u}^n+\mathbf{g}+\frac{1}{\rho(\phi^n)}(\nabla\cdot(\mu(\phi^n)\mathbf{S}^n)-\sigma\kappa(\phi^n)\delta(\phi^n)\nabla\phi^n) \tag{20}$$

using the definition of the material derivative $D(\mathbf{u}_i)/Dt:=\partial_t(\mathbf{u}_i)+(\mathbf{u}_i\cdot\nabla)\mathbf{u}_i$. The superscript n indicates the respective time step. With this definition, we can rewrite the time-discrete Navier–Stokes equations as

$$\frac{\mathbf{u}^{n+1}-\mathbf{u}^*}{\delta t}+\frac{\nabla p^{n+1}}{\rho(\phi^{n+1})}=0 \tag{21}$$

$$\nabla\cdot\mathbf{u}^{n+1}=0 \tag{22}$$

Note that the LS function ϕ^{n+1} at time step $n+1$ must be available for the definition of (21). To this end, we must solve (19) for the $(n+1)$th time step prior to the treatment of (21), see the next section for the construction of ϕ^{n+1}.

Now, we apply the negative divergence operator to Equation (21), and with (22) we arrive at the pressure Poisson equation with the inverse density field as diffusion coefficient

$$-\nabla\cdot\left(\frac{1}{\rho(\phi^{n+1})}\nabla\hat{p}^{n+1}\right)=-\nabla\cdot\mathbf{u}^* \tag{23}$$

where $\hat{p}^{n+1}:=\delta t p^{n+1}$. We obtain an appropriate boundary conditions[‡] for the pressure Poisson equation by projecting the vector equation (21) onto the outer unit normal of the domain boundary

$$\left.\frac{\partial p^{n+1}}{\partial\mathbf{n}}\right|_\Gamma=\frac{\rho}{\delta t}(\mathbf{u}_\Gamma^*-\mathbf{u}_\Gamma^{n+1})\cdot\mathbf{n}$$

Thus, if we require $\mathbf{u}_\Gamma^{n+1}=\mathbf{u}_\Gamma^*$, we obtain homogeneous Neumann boundary conditions for the pressure

$$\left.\frac{\partial\hat{p}^{n+1}}{\partial\mathbf{n}}\right|_\Gamma=0$$

To ensure the existence of a solution, we also need to fulfill the compatibility condition

$$0=\int_\Omega\nabla\cdot\mathbf{u}\,\mathrm{d}\mathbf{x}=\int_\Gamma\mathbf{u}\cdot\mathbf{n}\,\mathrm{d}s$$

[‡]The construction of boundary conditions for the pressure Poisson equation is in general more involved [48]. However, since we are interested mainly in convection-dominated flows, the use of natural boundary conditions is reasonable.

DOI: 10.1002/fld

which expresses the fact that the velocity on the boundary Γ must have a vanishing total flux. Note that the employed space discretization must comply with this requirement. Now, we can solve the system (23) for $\hat{p}^{n+1} = \delta t p^{n+1}$ at least up to a constant. We fix this remaining degree of freedom in the pressure p^{n+1} via the additional condition

$$\int_\Omega p^{n+1} \, \mathrm{d}\mathbf{x} = 0$$

to ensure the comparability of the pressure results at different times t_n. Finally, we obtain a correction of the intermediate velocity field $\mathbf{u}^*$, such that the velocities at time t_{n+1}

$$\mathbf{u}^{n+1} = \mathbf{u}^* - \frac{1}{\rho(\phi^{n+1})} \nabla \hat{p}^{n+1} \tag{24}$$

are now divergence free.

The extension of Chorin's projection method to higher-order multi-step time discretizations is straightforward. Throughout this paper we use a second-order Adams–Bashford scheme for the integration of the momentum equation (20), i.e.

$$\frac{\mathbf{u}^* - \mathbf{u}^n}{\delta t_n} = \frac{1}{2} \left(\frac{\delta t_n + 2\delta t_{n-1}}{\delta t_{n-1}} L^n - \frac{\delta t_n}{\delta t_{n-1}} L^{n-1} \right) \tag{25}$$

where $\delta t_n = t_n - t_{n-1}$ denotes the length of the nth time step and L^n the right-hand side of (20) evaluated at time t_n. Note finally that the generalization of the projection approach to other integration schemes like a TVD Runge-Kutta method is somewhat more involved since we must ensure that the respective sub-step velocities are divergence free.

3.2. Time discretization and the LS function

In the following we consider the time discretization of the transport equation (19) for the LS function ϕ and its effect on the signed distance property of ϕ. The discretization is based on a second-order Adams–Bashford scheme (25) for time discretization and a fifth-order WENO scheme [49, 50] for the discretization of the convective term $\mathbf{u}^n \cdot \nabla \phi^n$. Furthermore, we use a third-order Lagrange interpolation scheme for the evaluation of the velocities at the cell centers.

Note that in general the transport of the LS function ϕ due to (19) will destroy its signed distance property. This property, however, is essential for the stable approximation of surface tension. Hence, a transported LS function should not be used directly for the approximation of curvature or the surface tension. Instead, we refer to the transported LS function as an intermediate LS function ϕ^*; i.e. the time-stepping scheme gives ϕ^* and not ϕ^{n+1} so that

$$\phi^* = \phi^n + \frac{1}{2} \left(\frac{\delta t_n + 2\delta t_{n-1}}{\delta t_{n-1}} u^n \cdot \nabla \phi^n - \frac{\delta t_n}{\delta t_{n-1}} u^{n-1} \cdot \nabla \phi^{n-1} \right) \tag{26}$$

To obtain a valid signed distance function ϕ^{n+1} from ϕ^* a reinitialization must be employed. There exist a number of variants for the reinitialization of the LS function; the one we employ in our implementation is essentially due to Sussman *et al.* [28]. Here, we give a short review of this scheme for the sake of completeness.

DOI: 10.1002/fld

Consider a given function $\phi^*(\mathbf{x})$ whose zero LS is the fluid interface. To generate the appropriate signed distance function $\phi^{n+1}(\mathbf{x})$ with an approximately identical zero LS as $\phi^*(\mathbf{x})$, we discretize the following pseudo-transient Hamilton–Jacobi problem

$$\partial_\tau d + \operatorname{sign}(\phi^*)(|\nabla d| - 1) = 0 \tag{27}$$

and evolve it to steady state with the initial value $d(\mathbf{x}, 0) = \phi^*(\mathbf{x})$. Note that the term $\operatorname{sign}(\phi^*)|\nabla d|$ can be interpreted as motion along the normal direction away from the zero LS. Since our numerical approach relies on the signed distance property in the vicinity of the free surface only it is sufficient to compute the solution of (27) in an $\varepsilon(\mathbf{x})$-neighborhood of the zero LS. This is also the region where the largest deviation from the exact signed distance occurs due to the transport of the LS function. The parameter $\varepsilon(\mathbf{x})$ must be chosen with respect to the spatial resolution of the employed numerical scheme, see the next section. The Hamilton–Jacobi reinitialization (27) is discretized using a third-order TVD Runge–Kutta [51] method in time and a fifth-order WENO scheme in space.

For the numerical treatment of (27) it is advisable to employ a regularized signum function since this leads to better conservation properties as well as a more stable approximation.[§] There exist various different regularization approaches, e.g. [28, 32]. In our implementation we employ the regularized signum function

$$\widetilde{\operatorname{sign}}(\phi^*) = \frac{\phi^*}{\sqrt{(\phi^*)^2 + |\nabla \phi^*|^2 (\delta x^2)}} \tag{28}$$

due to Peng *et al.* [32]. In the discrete setting the parameter δx is replaced by the spatial mesh-width h, see Section 3.3. Since (28) takes the gradient of ϕ^* into account we obtain the discrete conservation of the sign of the LS function (in the grid nodes). Note that the smoothed signum function (28) needs to be updated before each Euler-substep in the Runge–Kutta scheme.

To further improve the conservation properties of our method we employ an additional Picard iteration

$$\phi^{n+1} \leftarrow \phi^{n+1} + \omega(V_1(\phi^0) - V_1(\phi^{n+1})) \tag{29}$$

where $V_1(\phi^0)$ denotes the initial volume of Ω_1^0 and $V_1(\phi^{n+1}) := \int_\Omega H(\phi^{n+1})\,\mathrm{d}x$ is the volume of Ω_1^{n+1} after the reinitialization step to enforce the conservation of mass globally over time. Note that the choice of the damping parameter $\omega \leqslant 1$ has a substantial impact on the speed of convergence of iteration (29). Here, the main influence on ω is the topology of the two fluid phases, i.e. the curvature of Γ_f.

3.3. Space discretization

Let us now consider the numerical treatment of the momentum equation. To this end, we need to specify the spatial discretization scheme. Here, we employ a widely used finite difference/finite volume scheme on a staggered grid to discretize the velocity field $\mathbf{u} := (u, v, w)^{\mathrm{T}}$ and the pressure p; i.e. the cell centers $x_{i,j,k}$ correspond to the pressure nodes, whereas the cell-face centers

[§] Note that this regularization scheme is independent of the smoothing of the material parameters given in Section 3.4, which is required for the treatment of surface tension effects only. However, we *always* use a regularized signum function.

DOI: 10.1002/fld

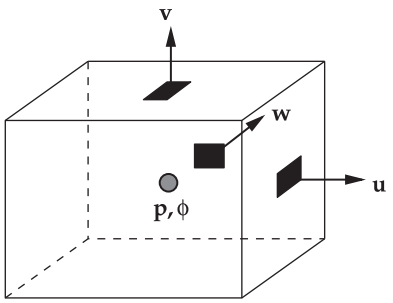

Figure 3. Location of variables in a staggered grid cell.

$x_{i+1/2,j,k}$, $x_{i,j+1/2,k}$, and $x_{i,j,k+1/2}$ give the velocity nodes for u, v, and w, respectively, see e.g. [6]. Furthermore, we discretize the LS function ϕ in the pressure nodes, see Figure 3. Note that all discrete fields are denoted by a subscript h, e.g. the discrete velocity in the x-direction is given by u_h and the discrete LS function by ϕ_h.

The computation of the discrete intermediate velocity $\mathbf{u}_h^*$ in (20) requires the discretization of the viscous terms $\nabla\cdot(\mu(\phi_h^n)\mathbf{S}_h^n)$ in the velocity nodes of the staggered grid. Since the velocities are continuous for viscous fluids (and due to the use of a smoothed viscosity, compare (30)) the first and second-order derivatives are approximated with central differences. Note however that we need to employ an appropriate interpolation scheme to evaluate the discrete LS function ϕ_h in all velocity nodes, i.e. in the cell-face centers, since ϕ_h is itself given in the pressure nodes, i.e. in the cell centers. To this end, we use a third-order Lagrange interpolation scheme.

To be able to treat convection-dominated flow problems, it is essential to employ a higher-order discretization for the convective terms. Here, we use a fifth-order WENO scheme [49, 50] for the treatment of all convective terms, see [52] for details. This approach yields a very good conservation properties even in the presence of large velocity gradients and allows for a stable approximation of the curvature. Note that an appropriate interpolation scheme for the velocities is required to apply the employed fifth-order WENO scheme. Again, we use a third-order Lagrange interpolation.[¶]

3.4. Smoothing, surface tension, surface normals, and curvature

So far we have neglected the discontinuity of the density at the interface. Yet, a jump in the diffusion coefficient in (23) can have a substantial adverse effect on the stability and the accuracy of our numerical scheme. Hence, we need to develop an appropriate smoothing scheme for the material properties, so that the density and the viscosity are at least continuous across the interface. This smoothing scheme, however, should not affect the approximation properties globally. Another challenge here is of course the discretization of the Dirac delta functional introduced by the CSF-approach. In general the main issue in the discretization of a CSF formulation is the introduction of the so-called parasitic currents [14] that also arise in our approach. To our knowledge; however,

[¶]At the boundary of the computational domain we use a right- or left-weighted Lagrange interpolation. Note that for the evaluation of this higher-order interpolation scheme some velocity values first need to be interpolated in the cell-face centers. Here, we use a two-dimensional Lagrange interpolation of third order. Close to the boundary, we employ a bilinear interpolation.

DOI: 10.1002/fld

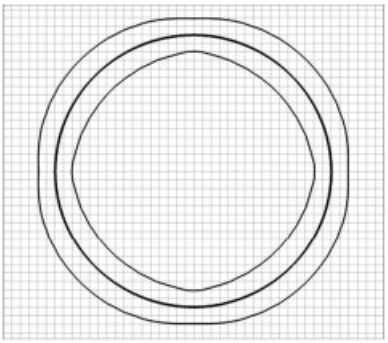

Figure 4. Numerical smoothing region defined in (33) with $c_\alpha = 2$ for a spherical droplet.

there is no discrete formulation of the CSF method that completely avoids this issue and a detailed analysis [53, 54] of the impact of parasitic currents on the overall convergence behavior is an open question.

To this end, let us consider the interface as having the thickness $\varepsilon(\mathbf{x})$, which is proportional to the spatial mesh-width h, see Figure 4. Then, we replace the discrete density $\rho(\phi_h)$ and the discrete viscosity $\mu(\phi_h)$ by

$$\rho^\varepsilon(\phi_h) = \rho_2 + (\rho_1 - \rho_2) H^\varepsilon(\phi_h) \quad \text{and} \quad \mu^\varepsilon(\phi_h) = \mu_2 + (\mu_1 - \mu_2) H^\varepsilon(\phi_h) \tag{30}$$

where H^ε denotes a smoothed Heaviside function

$$H^\varepsilon(\phi_h(\mathbf{x})) := \begin{cases} 0 & \text{if } \phi_h(\mathbf{x}) < -\varepsilon(\mathbf{x}) \\ \dfrac{1}{2}\left(1 + \dfrac{\phi_h(\mathbf{x})}{\varepsilon} + \dfrac{1}{\pi}\sin\left(\dfrac{\pi\phi_h(\mathbf{x})}{\varepsilon(\mathbf{x})}\right)\right) & \text{if } |\phi_h(\mathbf{x})| \leqslant \varepsilon(\mathbf{x}) \\ 1 & \text{if } \phi_h(\mathbf{x}) > \varepsilon(\mathbf{x}) \end{cases} \tag{31}$$

The associated smoothed delta functional is given by the derivative of (31), i.e.

$$\delta^\varepsilon(\phi_h(\mathbf{x})) := \partial_{\phi_h} H^\varepsilon(\phi_h(\mathbf{x})) = \begin{cases} \dfrac{1}{2\varepsilon(\mathbf{x})}\left(1 + \cos\left(\dfrac{\pi\phi_h(\mathbf{x})}{\varepsilon(\mathbf{x})}\right)\right) & \text{if } |\phi_h(\mathbf{x})| \leqslant \varepsilon(\mathbf{x}) \\ 0 & \text{else} \end{cases} \tag{32}$$

According to [55] a space- and ϕ_h-dependent smoothing region must be employed to account for mesh-alignment effects. We employ the smoothing region $|\phi_h(\mathbf{x})| \leqslant \varepsilon(\mathbf{x})$ with

$$\varepsilon(\mathbf{x}) = \alpha(\mathbf{x}) h \quad \text{where } \alpha(\mathbf{x}) := c_\alpha \frac{\|\nabla\phi_h(\mathbf{x})\|_1}{\|\nabla\phi_h(\mathbf{x})\|_2} < C \tag{33}$$

with $c_\alpha = 1.5$ in our implementation.

The fundamental assumption for the above smoothing scheme is that the gradient of the LS function is constant in the $\varepsilon(\mathbf{x})$ region; i.e. that the contours of ϕ_h in the $\varepsilon(\mathbf{x})$ region are symmetric to the zero LS. Owing to the choice of a signed distance function in our implementation this assumption is automatically satisfied.

DOI: 10.1002/fld

Note that we employ the smoothed Heaviside function in the approximation of the volumes $V_1(\phi^0)$ and $V_1(\phi^{n+1})$ in the iteration (29). The respective integrals $\int_\Omega H^\varepsilon(\phi_h)\,\mathrm{d}x$ are approximated by a simple midpoint integration rule and we employ a damping of $\omega = 0.1$ throughout this paper.

The use of the smoothed delta functional (32) reduces the quality of the approximation locally within the smoothing region by one order. To this end, consider a function g and its approximation g_h with a pointwise approximation error $g - g_h$ of order $O(h^p)$. Then, the smoothed error $(g - g_h)\delta^\varepsilon$ is of the order $O(h^p)O(\varepsilon(\mathbf{x})^{-1}) \approx O(h^{p-1})$ since $\varepsilon(\mathbf{x}) \approx h$.

Finally, we must consider the approximation of the surface tension for the overall discretization of the momentum equation (17). Recall that the surface tension force enters as a singular source term which we converted to a volume integral using a delta functional and the CSF-approach. Hence, the main ingredient in the approximation of the surface tension is the use of the smoothed delta functional $\delta^\varepsilon(\phi_i)$ given in (32) with ε defined in (33). This leads to a volumetric approximation of the surface tension force with support in the ε-neighborhood of the free surface, i.e.

$$\sigma\kappa\delta(\phi)\mathbf{n} \approx \sigma\kappa_h\delta^\varepsilon(\phi_h)\mathbf{n}_h$$

Recall that the discrete unit normal $\mathbf{n}_h$ on the interface is given by $\mathbf{n}_h := \nabla\phi_h/|\nabla\phi_h|$ and the discrete curvature in three dimensions is defined as $\kappa_h := \nabla\cdot\mathbf{n}_h$. Note that even though we employ a signed distance function, i.e. $|\nabla\phi_h| = 1$ in the ε-neighborhood of the free surface, we compute $\mathbf{n}_h$ by $\nabla\phi_h/|\nabla\phi_h|$ rather than just by $\nabla\phi_h$. Similarly, we compute the discrete curvature κ_h by $\nabla\cdot\mathbf{n}_h$ rather than by $\Delta\phi_h$. This procedure allows for a more stable approximation of the surface normals as well as the curvature at cusps. Note that all differential operators in these computations are approximated using central differences.

Now that the momentum equations are discretized, it remains to discretize the pressure Poisson equation

$$-\nabla\cdot\frac{1}{\rho^\varepsilon(\phi_h^{n+1})}\nabla\hat{p}_h^{n+1} = -\nabla\cdot\mathbf{u}_h^* \tag{34}$$

where $\rho^\varepsilon(\phi_h^{n+1})$ denotes the smoothed discrete density field (30) after the advection step (26), the reinitialization (27) and the fixed point iteration (29). Since the velocities of a viscous fluid flow are sufficiently smooth, we compute the right-hand side of (34) with central differences.

The left-hand side of (34) is discretized in three dimensions with a standard seven-point stencil in the cell centers where the smoothed density field is evaluated in the cell-face centers via an interpolated LS function. According to Section 3.1, we complement the pressure equation with homogeneous Neumann boundary conditions and enforce a vanishing mean for the pressure $p^{n+1} = (\delta t)^{-1}\hat{p}^{n+1}$. For the iterative solution of the resulting semi-definite diffusion equation we employ our parallel algebraic multigrid solver [56].

3.5. Adaptive time step control

Since we employ an explicit scheme for the velocities we have to deal with a time step restriction due to the CFL condition for explicit schemes. The CFL condition takes convection, viscosity, surface tension, and gravity into account and ensures that the discrete information can evolve no further than one grid cell since the discrete difference equations consider only fluxes between adjacent cells.

DOI: 10.1002/fld

With the definitions $u_{\max} := \max_{i,j,k} |u_{i+1/2,j,k}|$, $\kappa_{\max} := \max_{i,j,k} |\kappa_{i,j,k}|$, and

$$V := \max\left\{\frac{\mu_1}{\rho_1}, \frac{\mu_2}{\rho_2}\right\}\left(\frac{2}{(\delta x)^2}+\frac{2}{(\delta y)^2}+\frac{2}{(\delta z)^2}\right)$$

the overall time step restriction for the u-component of the velocity field can be expressed as

$$\delta t^u \leqslant 2C_u$$

where

$$C_u := \left(\left(\frac{u_{\max}}{\delta x}+V\right)+\sqrt{\left(\frac{u_{\max}}{\delta x}+V\right)^2+\frac{4|g_1|}{\delta x}+\frac{8\kappa_{\max}\sigma}{c_\alpha(\rho_2+\rho_1)(\delta x)^2}}\right)^{-1}$$

The bounds for δt^v and δt^w associated with the velocities in the y- and the z-direction involving C_v and C_w, respectively, are defined in an analogous way. Hence, we first obtain an appropriate time step restriction $\delta t^{u/v/w} \leqslant 2C_{u/v/w}$ for each velocity component separately. The final time step restriction can then be computed easily as the minimum of these three scalar bounds. This yields the overall time step restriction

$$\delta t \leqslant 2\xi \min_{\Omega}(C_u, C_v, C_w)$$

with a safety factor $\xi \in (0, 1]$. Throughout this paper, we employ this adaptive time step control using $\xi = 0.3$ in our computations.

4. NUMERICAL RESULTS

In this section we present the results of our numerical experiments in three space dimensions. First, we investigate the order of convergence obtained for the approximation of the curvature by means of a diagonally transported unit sphere. In particular, we analyze the effect of the LS reinitialization and the fixed point iteration on the convergence of the curvature and the mass conservation properties of our numerical scheme. Then we examine the global order of convergence to our overall numerical scheme for two-phase flow problems including surface tension on the basis of a rising bubble test problem. Finally, we consider the deformation of a liquid droplet due to a surrounding shear flow.

4.1. Mass conservation and convergence of curvature

First, we investigate the convergence behavior of our numerical scheme with respect to mass and curvature considering the simple test case of an advected unit sphere. Since the curvature of the unit sphere is known analytically, we can directly compare the approximated curvature with the exact solution.

To this end, we consider the domain $\Omega = [0, 4]^3$, which we discretize by a sequence of uniformly refined equidistant grids. Furthermore, we employ periodic boundary conditions on $\partial\Omega$ and a stationary velocity field

$$u(x, y, z) = 1, \quad v(x, y, z) = 1, \quad w(x, y, z) = 0$$

DOI: 10.1002/fld

As an initial condition for the LS function we use the analytic distance function

$$\phi(x,y,z)=1-\sqrt{(x-2)^2+(y-2)^2+(z-2)^2} \tag{35}$$

whose zero LS is a sphere with radius $r=1$ centered at $(2,2,2)$; i.e. we transport the sphere over time along the diagonal in the xy-plane.

In this experiment we consider four different configurations of our numerical scheme to distinguish the effects on the convergence behavior associated with the reinitialization step and the fixed point iteration; i.e. we perform the simulation with/without reinitialization (27) and with/without fixed point iteration (29).

Recall that the curvature is defined as

$$\kappa_h(\phi_h)(\mathbf{x})=\nabla\cdot\frac{\nabla\phi_h(\mathbf{x})}{\|\nabla\phi_h(\mathbf{x})\|}$$

Let us furthermore define the following discrete error norms

$$e_\varepsilon^{\kappa,h}(\mathbf{x}):=\frac{|\kappa_h(\phi_h)(\mathbf{x})-\kappa(\phi)(\mathbf{x})|}{|\kappa(\phi)(\mathbf{x})|}\quad\text{with }\kappa(\phi)(\mathbf{x}):=\frac{2}{1-\phi(\mathbf{x})} \tag{36}$$

$$e_{\varepsilon,1}^{\kappa,h}:=\sum_{\mathbf{x}_i,|\phi_h(\mathbf{x}_i)|<\alpha(\mathbf{x}_i)h} e_\varepsilon^{\kappa,h}(\mathbf{x}_i) \tag{37}$$

$$e_{\varepsilon,\infty}^{\kappa,h}:=\max_{\mathbf{x}_i,|\phi_h(\mathbf{x}_i)|<\alpha(\mathbf{x}_i)h} e_\varepsilon^{\kappa,h}(\mathbf{x}_i) \tag{38}$$

in the $\varepsilon(\mathbf{x})$ region given by $|\phi_h(\mathbf{x}_i)|<\alpha(\mathbf{x}_i)h=\varepsilon(\mathbf{x})$ (compare (33). Thus, we measure the error not only on the interface, but also near the interface. Note that we do not employ the smoothed delta functional δ^ε in this computation. Recall that δ^ε is required only for the evaluation of surface tension force; hence, it is not needed for the approximation of the curvature.

Furthermore, we measure the error with respect to the initial mass at time $t=4$ via the discrete norms

$$m_\varepsilon^{h,t}:=\sum_{\mathbf{x}_i,|\phi_h(\mathbf{x}_i)|<\alpha(\mathbf{x}_i)h} H^\varepsilon(\phi_h^t(\mathbf{x}_i))h^3,\quad e_\varepsilon^{m,h}:=\frac{|m_\varepsilon^{h,t}-m_\varepsilon^{h,0}|}{|m_\varepsilon^{h,0}|} \tag{39}$$

The respective algebraic convergence rates η are determined by

$$\eta:=-\frac{\log e^{2h}/e^h}{\log \mathsf{dof}_{2h}/\mathsf{dof}_h} \tag{40}$$

respectively.

Since we employ an absolute stopping criterion of 10^{-7} in the fixed point iteration we anticipate to find a constant error e_ε^m when the fixed point iteration is used independently of the reinitialization step. Owing to the fact that we employ a constant velocity field in this experiment the signed distance property of the LS function is only slightly disturbed over time so that we anticipate to find very similar results for the cases with/without reinitialization.

The results of our numerical study are summarized in Table I and Figures 5 and 6. The convergence rates η_ε^m are obtained with respect to the total number of grid cells dof, whereas the convergence rates η_ε^κ are determined with respect to the number of grid cells dof_ε in the $\varepsilon(\mathbf{x})$ region.

DOI: 10.1002/fld

Table I. Relative errors e and convergence rates η obtained for the curvature κ and mass m.

$1/h$	dof^h	$\mathsf{dof}_\varepsilon^h$	$e_{\varepsilon,1}^{\kappa,h}$	$\eta_{\varepsilon,1}^{\kappa,h}$	$e_{\varepsilon,\infty}^{\kappa,h}$	$\eta_{\varepsilon,\infty}^{\kappa,h}$	$e_\varepsilon^{m,h}$	$\eta_\varepsilon^{m,h}$
Reinitialization (−) *fixed point* (−)								
25	15625	2214	7.034_{-3}	—	3.890_{-2}	—	3.130_{-4}	—
50	125000	8928	1.288_{-3}	1.218	5.236_{-3}	1.438	1.521_{-4}	0.346
100	1000000	35376	3.119_{-4}	1.030	1.015_{-3}	1.192	4.823_{-5}	0.552
200	8000000	141440	7.773_{-5}	1.003	2.271_{-4}	1.080	1.244_{-5}	0.651
400	64000000	565768	1.943_{-5}	1.000	5.320_{-5}	1.047	3.123_{-6}	0.664
Reinitialization (+) *fixed point* (−)								
25	15625	2214	1.133_{-2}	—	4.370_{-2}	—	1.969_{-3}	—
50	125000	8932	1.437_{-3}	1.481	4.622_{-3}	1.611	4.652_{-6}	2.909
100	1000000	35380	3.128_{-4}	1.108	9.112_{-4}	1.180	4.289_{-5}	−1.068
200	8000000	141440	7.769_{-5}	1.005	2.147_{-4}	1.043	1.220_{-5}	0.604
400	64000000	565768	1.943_{-5}	0.999	5.180_{-5}	1.026	3.105_{-6}	0.658
Reinitialization (−) *fixed point* (+)								
25	15625	2214	7.034_{-3}	—	3.890_{-2}	—	8.338_{-9}	—
50	125000	8928	1.288_{-3}	1.218	5.236_{-3}	1.438	8.365_{-8}	−1.109
100	1000000	35376	3.120_{-4}	1.030	1.015_{-3}	1.192	7.702_{-8}	0.039
200	8000000	141436	7.773_{-5}	1.003	2.271_{-4}	1.080	9.244_{-8}	−0.087
400	64000000	565768	1.943_{-5}	1.000	5.320_{-5}	1.047	9.727_{-8}	−0.024
Reinitialization (+) *fixed point* (+)								
25	15625	2214	1.131_{-2}	—	4.373_{-2}	—	5.157_{-9}	—
50	125000	8932	1.437_{-3}	1.479	4.623_{-3}	1.611	8.952_{-8}	−1.373
100	1000000	35380	3.129_{-4}	1.107	9.113_{-4}	1.180	7.659_{-8}	0.075
200	8000000	141436	7.769_{-5}	1.005	2.147_{-4}	1.043	9.238_{-8}	−0.090
400	64000000	565768	1.943_{-5}	0.999	5.180_{-5}	1.026	9.725_{-8}	−0.024

Since $\mathsf{dof}_\varepsilon \approx h^{-2}$ the classical second-order convergence corresponds to $\eta = 1$. Analogously, we obtain classical second-order convergence for the mass if $\eta = \frac{2}{3}$ since $\mathsf{dof} \approx h^{-3}$.

From the numbers displayed in Table I and the plots displayed in Figures 5 and 6 we can clearly observe this anticipated optimal convergence behavior of our numerical scheme. As expected the error with respect to mass is constant $<10^{-7}$ if the fixed point iteration with absolute stopping criterion is used; i.e. we find the rate $\eta_\varepsilon^m \approx 0$ due to the absolute stopping criterion. The reinitialization (R+) has almost no effect on the convergence behavior in this example since the distance property of the LS function is well preserved over time due to the constant advection velocity.

4.2. Convergence for two-phase flow with surface tension

To determine the convergence behavior of the complete two-phase flow solver including surface tension, we now consider a rising bubble reference problem. Here, a spherical bubble of a lighter fluid rises and deforms in a denser fluid due to gravitational forces. The deformation behavior of the bubble is dominated by surface tension effects. Thus, we must consider surface tension forces in our numerical scheme, so that the smoothed delta functional δ^ε is employed in these computations. Furthermore, the deformation of the spherical bubble is substantial over time so that a re-initialization step must be employed to enforce the signed distance property of the LS function for all times. To cope with the loss of mass due to the re-initialization of the LS function

DOI: 10.1002/fld

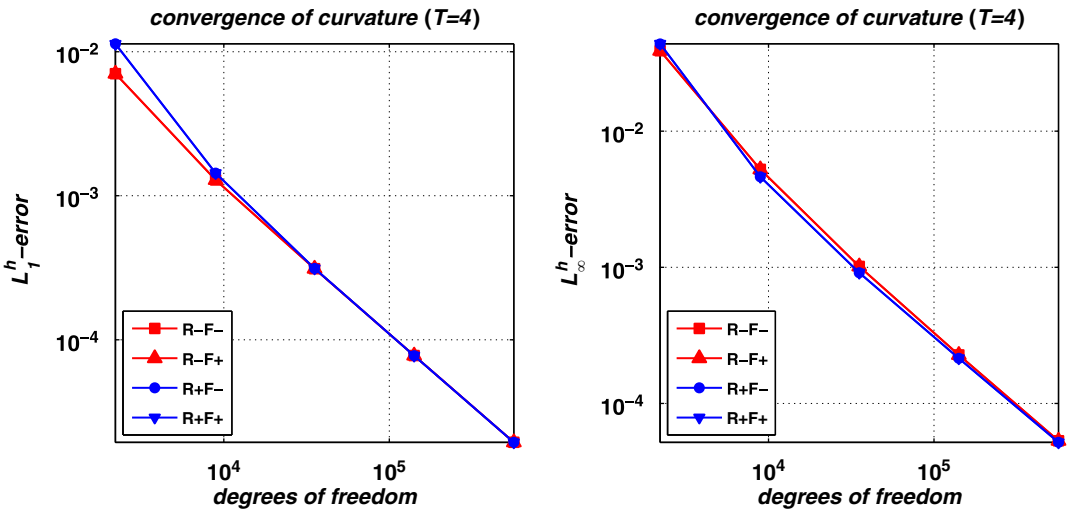

Figure 5. Convergence history of the curvature.

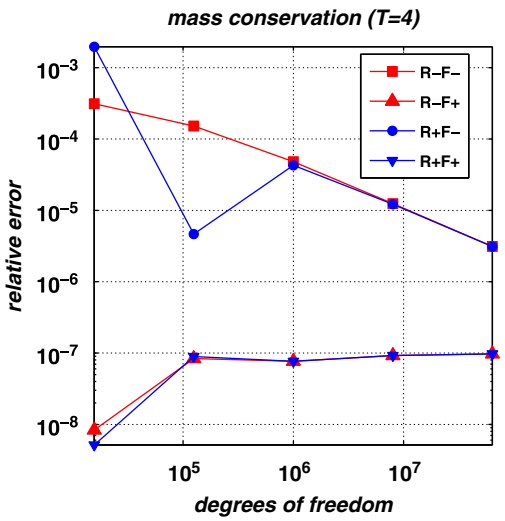

Figure 6. Convergence history for the relative error of mass.

we again employ a global fixed point iteration. For comparison we also give the results obtained without the fixed point iteration (Figure 7).

We anticipate to find the first-order convergence near the free surface due to the smoothing of the delta functional, whereas away from the free surface we expect to obtain a second-order approximation since there, the smoothed delta functional is not active. Hence, we expect to find a global approximation order close to two.

DOI: 10.1002/fld

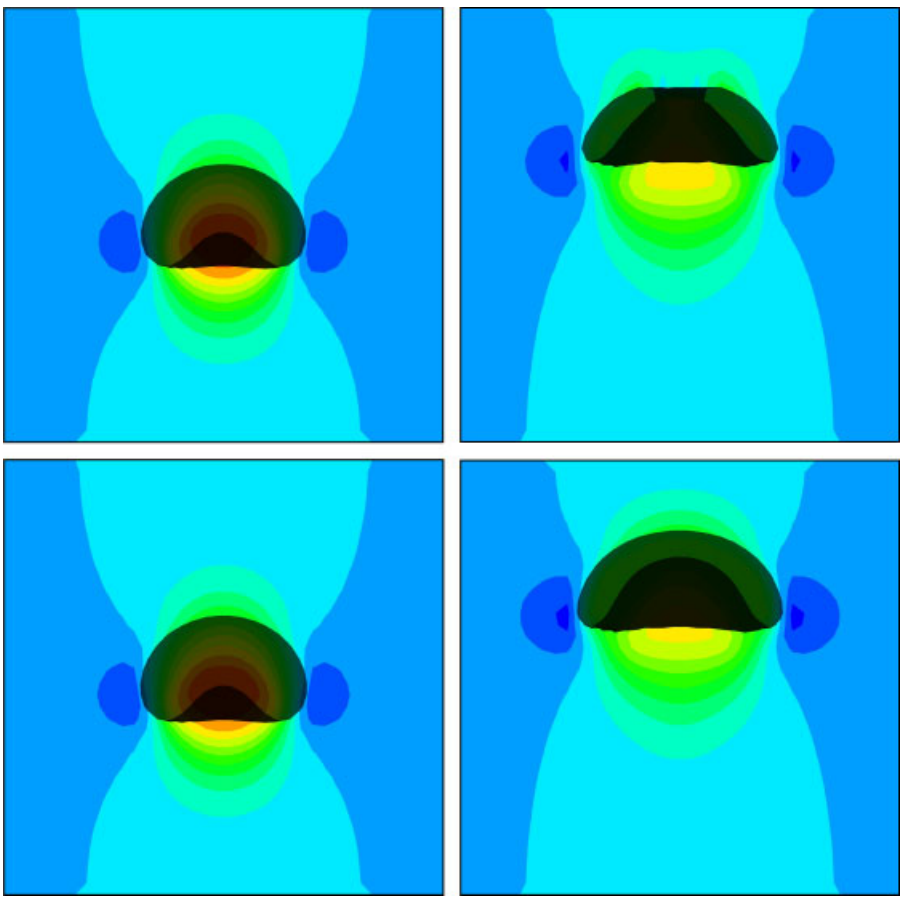

Figure 7. Rising bubble without (upper row) and with (lower row) fixed point iteration for improved mass conservation at times $t=0.075\,\mathrm{s}$ (left column) and $t=0.15\,\mathrm{s}$ (right column) for $h=\frac{1}{37}$. Depicted is a semi-transparent iso-surface of the zero-level set and a contour plot of the v-velocity along the center plane.

The physical properties of the considered fluids and the boundary conditions are given in Table II. The initial condition for the LS function ϕ corresponds to a spherical bubble with its center located at $(0.075\,\mathrm{m},\ 0.05\,\mathrm{m},\ 0.075\,\mathrm{m})$ and radius $r=0.025\,\mathrm{m}$. We consider the computational domain $\Omega=[0,0.15\,\mathrm{m}]^3$ which we discretize by three uniformly refined equidistant grids with mesh-width $h=\frac{1}{37},\frac{1}{73},\frac{1}{145}$ together with the equidistant time steps $\delta t_h=6.25_{-5},2.50_{-4},1.00_{-3}$, respectively. Furthermore, we employ a gravitational force $g=(0,-9.81,0)\,\mathrm{Nm}$.

Owing to the lack of an analytical solution we employ a reference solution computed on a grid with mesh-width $\frac{1}{289}$ to assess the quality of our numerical scheme. To this end we make the definitions

$$E_h^{\mathrm{ref}}(\psi_h) := I_h^{\mathrm{ref}}\psi_h - \psi_{\mathrm{ref}}$$

DOI: 10.1002/fld

Table II. Material parameters and boundary conditions employed in the rising bubble problem.

$\text{fluid}_1: \mu_1 = 2.5_{-4}\,\text{kg/ms},\ \rho_1 = 1.0_0\,\text{kg/m}^3$
$\text{fluid}_2: \mu_2 = 5.0_{-4}\,\text{kg/ms},\ \rho_2 = 1.0_1\,\text{kg/m}^3$
surface tension: $\sigma = 5.0_{-3}\,\text{N/m}$
boundary conditions: slip

Fluid_1 denotes the bubble and fluid_2 the surrounding fluid.

where I_h^{ref} denotes a tri-linear interpolation of the data computed on a mesh with mesh-width h to the reference mesh

$$\|\psi_{\text{ref}}\|_{L^2} := \frac{1}{N_{\text{ref}}} \left(\sum_{i=1}^{N_{\text{ref}}} |\psi_{\text{ref}}(\mathbf{x}_i)|^2 \right)^{1/2}, \quad \|\psi_{\text{ref}}\|_{L^\infty} := \max_{i=1,\ldots,N_{\text{ref}}} |\psi_{\text{ref}}(\mathbf{x}_i)|$$

and

$$e_{p,h}^{\psi} := \frac{\|E_h^{\text{ref}}(\psi_h)\|_{L^p}}{\|\psi_{\text{ref}}\|_{L^p}} \tag{41}$$

We consider the convergence of the velocities u_h, v_h, w_h, the LS function ϕ_h, and the pressure p_h in this experiment. Again we determine the algebraic convergence rates according to (40) so that classical second-order convergence is obtained if $\eta = \frac{2}{3}$. Since we must employ the smoothed delta functional to realize the surface tension in our simulation we cannot expect to find $\eta = \frac{2}{3}$ globally, but we anticipate to find η between $\frac{1}{3}$ and $\frac{2}{3}$ only. On finer grids we expect to find η being closer to $\frac{2}{3}$ due to the smaller discrete surface to volume ratio; i.e. the smaller impact of the smoothing of the delta functional.

The measured relative errors (41) and the respective convergence rates (40) are given in Tables III and IV. From the displayed numbers we can observe the anticipated convergence behavior. We find the convergence rates η between $\frac{1}{3}$ and $\frac{2}{3}$ approaching $\frac{2}{3}$ with decreasing mesh-width for the velocities with respect to the L^2-norm and the L^∞-norm. Furthermore, the results obtained for the u and w velocities are identical due to the symmetry of the problem. The relative errors and convergence rates attained for the LS function ϕ correspond very well to those of the velocities. Again we find η between $\frac{1}{3}$ and $\frac{2}{3}$ approaching $\frac{2}{3}$ on finer grids indicating a close to second-order convergence also for the LS function. The positive effect of the fixed point iteration on the mass conservation is clearly visible from the measured relative errors $e_{\varepsilon}^{m,h}$ given in Table IV. We obtain roughly five digits accuracy in mass with the fixed point iteration on all grids, whereas without the fixed point iteration we find only up to three digits accuracy. As expected, the convergence behavior of the pressure p is somewhat reduced due to the fact that the pressure is discontinuous across the interface.

4.3. Deformation of an air bubble in water

Next we consider a rising air bubble in water; thus, a two-phase flow problem with large jumps in the material parameters. To this end, we consider the three-dimensional version of a model problem studied in [39, 40]. The domain and initial fluid phases are $\Omega = (0, 0.2)\,\text{m} \times (0, 0.3)\,\text{m} \times (0, 0.2)\,\text{m}$,

DOI: 10.1002/fld

Table III. Convergence study for rising bubble problem at time $t=0.075$ s.

$1/h$	$e_\infty^{u,h}$	$\eta_\infty^{u,h}$	$e_2^{u,h}$	$\eta_2^{u,h}$	$e_\infty^{v,h}$	$\eta_\infty^{v,h}$	$e_2^{v,h}$	$\eta_2^{v,h}$	$e_\infty^{w,h}$	$\eta_\infty^{w,h}$	$e_2^{w,h}$	$\eta_2^{w,h}$
Fixed point (−)												
37	3.92_{-1}	—	2.08_{-1}	—	1.13_{-1}	—	1.09_{-1}	—	3.92_{-1}	—	2.08_{-1}	—
73	2.09_{-1}	0.31	8.47_{-2}	0.44	7.67_{-2}	0.19	4.92_{-2}	0.39	2.09_{-1}	0.31	8.47_{-2}	0.44
145	6.94_{-2}	0.54	2.60_{-2}	0.57	3.52_{-2}	0.38	1.59_{-2}	0.55	6.94_{-2}	0.54	2.60_{-2}	0.57
Fixed point (+)												
37	3.87_{-1}	—	2.04_{-1}	—	1.20_{-1}	—	1.11_{-1}	—	3.87_{-1}	—	2.04_{-1}	—
73	2.06_{-1}	0.31	8.35_{-2}	0.44	6.96_{-2}	0.27	5.01_{-2}	0.39	2.06_{-1}	0.31	8.35_{-2}	0.44
145	6.76_{-2}	0.54	2.56_{-2}	0.57	2.97_{-2}	0.41	1.60_{-2}	0.56	6.76_{-2}	0.54	2.56_{-2}	0.57

Table IV. Convergence study for rising bubble problem at time $t=0.075$ s.

$1/h$	$e_\varepsilon^{m,h}$	$\eta_\varepsilon^{m,h}$	$e_\infty^{\phi,h}$	$\eta_\infty^{\phi,h}$	$e_2^{\phi,h}$	$\eta_2^{\phi,h}$	$e_\infty^{p,h}$	$\eta_\infty^{p,h}$	$e_2^{p,h}$	$\eta_2^{p,h}$
Fixed point (−)										
37	4.621_{-2}	—	3.14_{-2}	—	1.89_{-2}	—	6.51_{-1}	—	1.14_{-2}	—
73	1.158_{-2}	0.679	1.27_{-2}	0.44	6.90_{-3}	0.50	5.89_{-1}	0.05	4.90_{-3}	0.41
145	2.402_{-3}	0.764	4.66_{-3}	0.49	2.19_{-3}	0.56	4.26_{-1}	0.16	1.92_{-3}	0.45
Fixed point (+)										
37	4.035_{-5}	—	3.49_{-2}	—	1.48_{-2}	—	6.52_{-1}	—	1.04_{-2}	—
73	2.343_{-5}	0.267	1.32_{-2}	0.48	6.32_{-3}	0.42	5.90_{-1}	0.05	4.55_{-3}	0.41
145	6.541_{-6}	0.620	4.46_{-3}	0.53	2.15_{-3}	0.52	4.27_{-1}	0.16	1.82_{-3}	0.45

bubble radius $r_0=\frac{1}{30}$ m and center (0.1 m, 0.1 m). The gravitational force and material properties are $g=(0,-9.8,0)\,\mathrm{m/s^2}$, $\sigma=0.0728\,\mathrm{N/m}$, $\rho_{\mathrm{water}}=10^3\,\mathrm{kg/m^3}$, $\rho_{\mathrm{air}}=1.226\,\mathrm{kg/m^3}$, $\mu_{\mathrm{water}}=1.137\times 10^{-3}\,\mathrm{kg/ms}$, and $\mu_{\mathrm{air}}=1.78\times 10^{-5}\,\mathrm{kg/ms}$. We employ no-slip boundary conditions on $\partial\Omega$.

In Figure 8 we give the interface positions at times $t=0.01$ s, 0.02 s, 0.035 s, and 0.05 s on three different meshes. These results compare very well with those of [39, 40] up to $t=0.035$ s and the results on the three considered meshes are almost identical. For later times $t\geqslant 0.035$ when the bubble is substantially deformed from its initial state we clearly see the improvement in the simulation due to mesh refinement. Our results however for $t\geqslant 0.035$ are quite different from those of [39, 40], which are due to the fact that we consider a three-dimensional setting where the surface to volume ratio is smaller than in two dimensions. To confirm this assertion, we also simulated the quasi-two-dimensional analogue with periodic boundary conditions in the z-direction; i.e. we consider a rod-shaped bubble. The computed results are presented in Figure 9.

Comparing our results of Figure 9 with the two-dimensional simulation of [40] obtained for the ghost fluid method, we find a very good agreement up to $t\leqslant 0.035$. For later times $t>0.035$ the loss of mass that occurs in the ghost fluid method of [40] is becoming substantial and hence yields a deterioration of the quality of the simulation. Our scheme however ensures mass conservation so that even long-time simulations can be carried out reliably. The numerical approach presented in [39] also attains mass conservation, but there a first-order transport of the LS function is only employed, which again spoils the quality of long-time simulations. In our approach we employ a

DOI: 10.1002/fld

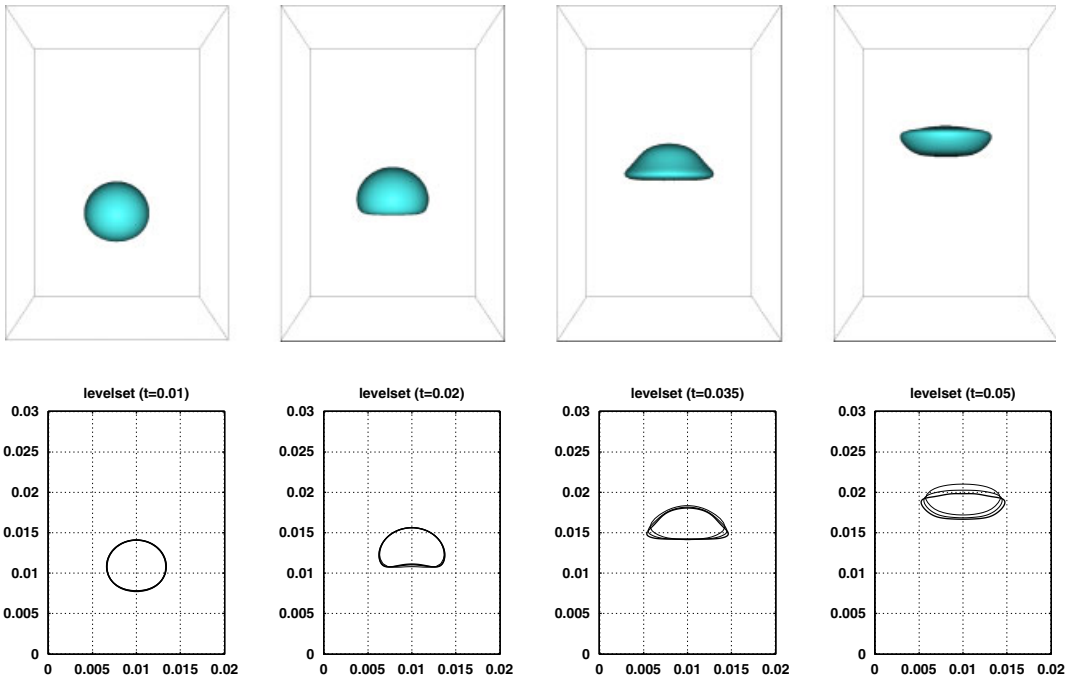

Figure 8. Air bubble rising in water at times $t=0.01$ s, 0.02 s, 0.035 s, and 0.05 s (left to right). Depicted in the top row are the interface positions for mesh-width$=(\frac{1}{160}, \frac{1.5}{240}, \frac{1}{160})$. On the bottom row we give the intersections of the interface with the center plane of the computational domain for the mesh-widths$=(\frac{1}{40}, \frac{1.5}{60}, \frac{1}{40})$, $(\frac{1}{80}, \frac{1.5}{120}, \frac{1}{80})$, and $(\frac{1}{160}, \frac{1.5}{240}, \frac{1}{160})$ (bold line corresponds to finest resolution).

higher-order transport scheme. Thus, we attribute the differences of our results to those of [39] for later times $t>0.035$ to this superior transport step.

In summary, the results presented in Figures 8 and 9 clearly show the need for three-dimensional simulations of bubble dynamics. The bubble depicted in Figure 8 is substantially faster and undergoes a different deformation pattern than its two-dimensional counterpart given in Figure 9, which is due to the difference in the surface to volume ratio and the stronger interaction with the boundary in two dimensions.

4.4. Deformation of a droplet in shear flow

Let us finally apply the presented numerical scheme to compute the deformation of a small droplet submitted to a shearing flow. To this end, we consider the idealized but representative reference problem of a circular drop with radius r_D sheared by a surrounding velocity field [16–18]. Here, the deformation behavior depends on the material properties of the two considered fluids and the employed shear rate $\dot{\gamma}$. For instance, we can obtain a steady-state solution with a deformed (close to) elliptical droplet geometry in the case of sufficiently large surface tension force. On the other hand, if the surface tension force is too small to cope with the counteracting forces imposed by

DOI: 10.1002/fld

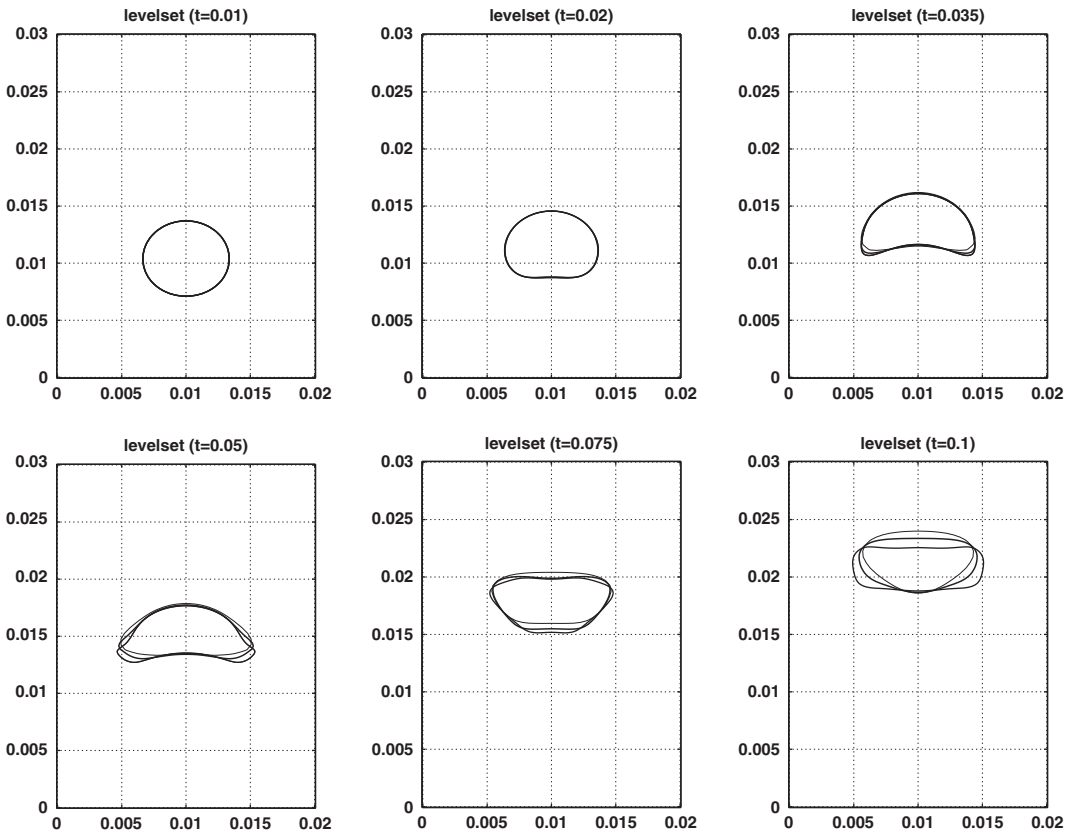

Figure 9. Quasi-2D air bubble rising in water at times $t = 0.01\,\text{s}$, $0.02\,\text{s}$, $0.035\,\text{s}$, $0.05\,\text{s}$, $0.075\,\text{s}$, and $0.1\,\text{s}$. We give the intersections of the interface with the center plane of the computational domain for the mesh-widths=$(\frac{1}{40}, \frac{1.5}{60}, \frac{1}{4})$, $(\frac{1}{80}, \frac{1.5}{120}, \frac{1}{8})$, and $(\frac{1}{160}, \frac{1.5}{240}, \frac{1}{16})$ (bold line corresponds to finest resolution).

the shear flow, the droplet undergoes a change in topology and may be ruptured and breaks into daughter droplets [16].

Let us denote the viscosity of the surrounding fluid by v_M and the viscosity of the droplet by v_D. The characteristic non-dimensional parameter of such a problem is the capillary number

$$Ca := \frac{\dot{\gamma} v_M r_D}{\sigma} \tag{42}$$

The capillary number is a measure of the shear stress relative to the surface tension. The deformation behavior of the droplet is qualitatively determined by the capillary number Ca and the Reynolds number Re of the flow. According to [16] there are two flow regimes: a stationary regime (SCT) where the droplet attains its initial topology, and an instationary regime (ITC) where the droplet undergoes topological changes and is ruptured into daughter droplets over time, see Figure 10.

DOI: 10.1002/fld

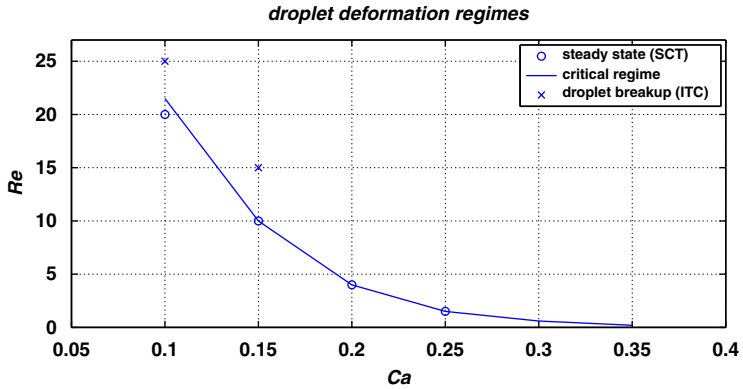

Figure 10. Phase diagram of droplet deformation with respect to the capillary number Ca and Reynolds number Re. The stationary regime with constant topology is indicated by SCT, the instationary regime where topological changes occur is indicated by ITC.

First, we consider four representative parameter settings for the SCT-regime with Reynolds numbers just below the respective critical values, namely $(Ca, Re) = (0.25, 1.5)$, $(0.2, 4)$, $(0.15, 10)$, and $(0.1, 20)$.[‖] We use periodic boundary conditions in horizontal direction and set $\mathbf{v} = (\pm 1, 0, 0)\,\mathrm{m/s}$ on the top/bottom domain boundary, i.e. $\dot{\gamma} = 2$. Note that these parameter choices were also considered in [16, 17] using a VOF scheme. The final stationary results obtained for these settings are given in Figures 11 and 12. These results compare very well with those of [16, 17]. With increasing Reynolds number we also find a loss of symmetry of the droplet across the mid-plane and a stronger deviation of the droplet's geometry from an ellipsoidal shape. Furthermore, the flow field inside the droplet develops multiple vortices with increasing Reynolds numbers, e.g. we find just a single vortex for $(Ca, Re) = (0.25, 1.5)$ and $(Ca, Re) = (0.2, 4)$ and two vortices for the cases of $(Ca, Re) = (0.15, 10)$ and $(Ca, Re) = (0.1, 20)$.

Let us now consider several configurations from the instationary ITC regime. The results obtained for the parameter $(Ca, Re) = (0.15, 15)$, i.e. $(\mu, \rho, \sigma) = (0.006\,\mathrm{kg/ms},\ 1.44\,\mathrm{kg/m^3}, 0.01\,\mathrm{N/m})$, are given in Figure 13. Here, the droplet is stretched from spheroidal to ellipsoidal shape, then to a dumbbell shape before it is ruptured into two daughter droplets. These daughter droplets then converge to a steady state with respect to topology since surface tension is large enough to prevent further break-up in this parameter setting.

For the parameters $(Ca, Re) = (0.1, 25)$, i.e. $(\mu, \rho, \sigma) = (0.001\,\mathrm{kg/ms},\ 0.4\,\mathrm{kg/m^3},\ 0.000625\ \mathrm{N/m})$, we anticipate to find a rupture of the droplet into more and smaller droplets over time since the balance of the surface tension and shear stress is valid up to the large deformation. Thus, rupture occurs after this elongation phase for a strongly stretched dumbbell-shaped droplet. Here, the ends pinch off and two rather large satellite droplets are spawned whose deformation behavior is similar to the initial droplet. The surrounding shear flow further elongates these three droplets and leads to further rupture of each of these droplets into smaller daughter droplets. This principal

[‖]The respective material parameters employed in the computations are $(\mu, \rho, \sigma) = (0.005\,\mathrm{kg/ms}, 0.12\,\mathrm{kg/m^3}, 0.005\,\mathrm{N/m})$, $(0.005\,\mathrm{kg/ms},\ 0.32\,\mathrm{kg/m^3},\ 0.00625\,\mathrm{N/m})$, $(0.006\,\mathrm{kg/ms},\ 0.96\,\mathrm{kg/m^3},\ 0.01\,\mathrm{N/m})$, and $(0.001\,\mathrm{kg/ms},\ 0.32\,\mathrm{kg/m^3},\ 0.0025\,\mathrm{N/m})$. There is no jump in the material parameters across the interface [16, 17].

DOI: 10.1002/fld

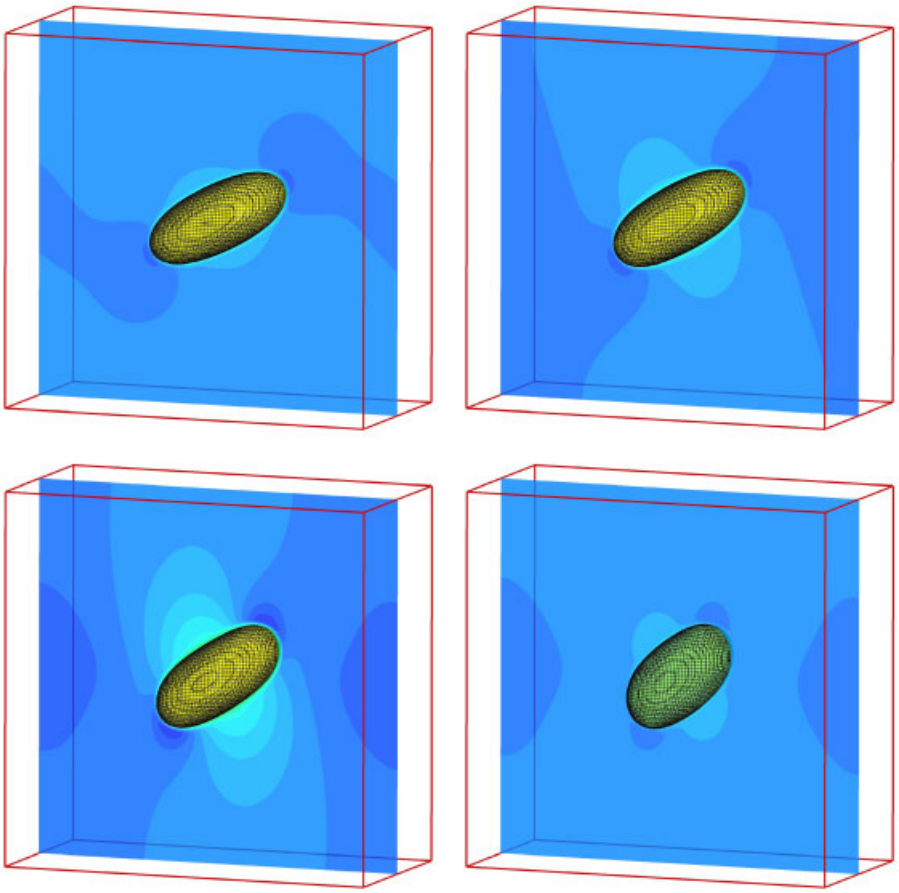

Figure 11. Stationary results obtained for the four parameter settings $(Ca, Re) = (0.25, 1.5)$, $(0.2, 4)$, $(0.15, 10)$, and $(0.1, 20)$ (top left to bottom right). Depicted are the configurations of the free surface in the stationary limit. The respective pressure fields are color coded employing the same scaling in all plots. The stationary limits are reached at the dimensionless times $t^* = 203.34$, $t^* = 538.41$, $t^* = 829.68$, and $t^* = 1649.36$ (top to bottom). The simulation domain is $2 \times 1 \times 2$ and the droplet has a radius of $r = 0.25$. The mesh-width is $(\frac{2}{128}, \frac{1}{64}, \frac{2}{128})$.

process continues until surface tension effects dominate the deformation behavior of the resulting daughter droplets; i.e. when the surface tension is larger than the shear stress. This anticipated behavior is clearly observable from the contour plots given in Figure 14.

5. CONCLUDING REMARKS

In this paper we presented an incompressible Navier–Stokes solver for two-phase flow problems with surface tension in three dimensions. One of the main concerns of our study was the impact

DOI: 10.1002/fld

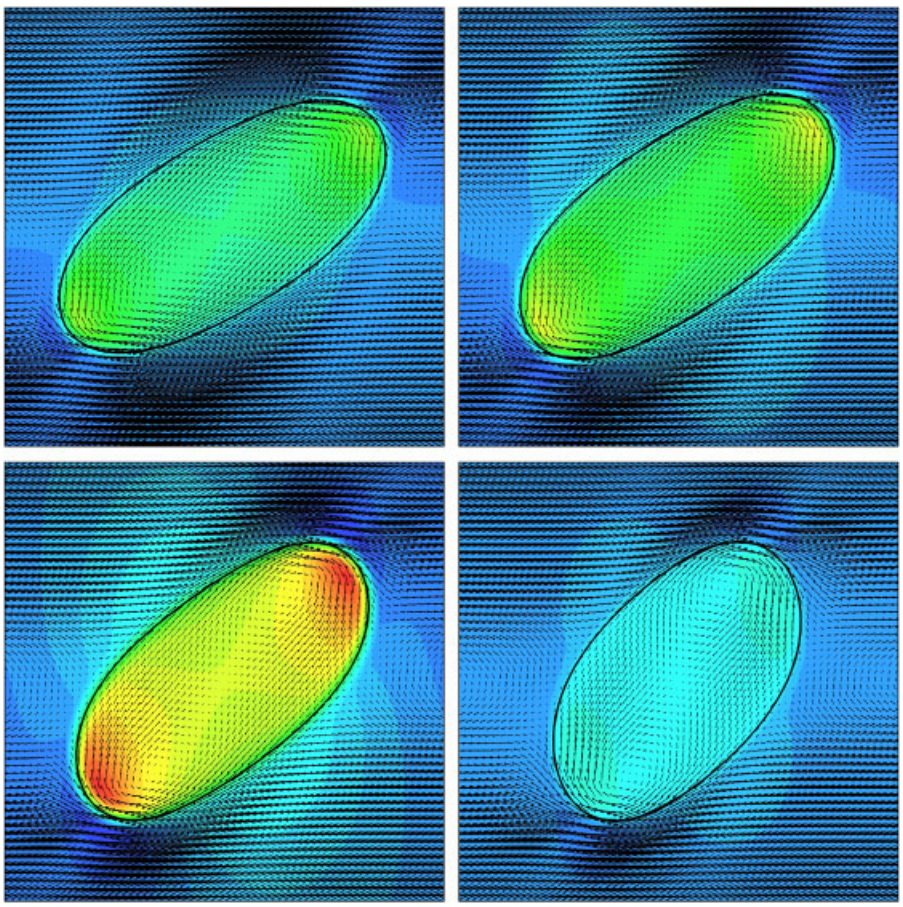

Figure 12. Stationary results obtained for the four parameter settings $(Ca, Re) = (0.25, 1.5)$, $(0.2, 4)$, $(0.15, 10)$, and $(0.1, 20)$ (top left to bottom right). Depicted are zooms of the free surface in the surrounding flow field along the center plane (right). The respective pressure fields are color coded employing the same scaling in all plots. The stationary limits are reached at the dimensionless times $t^* = 203.34$, $t^* = 538.41$, $t^* = 829.68$, and $t^* = 1649.36$ (top to bottom). The simulation domain is $2 \times 1 \times 2$ and the droplet has a radius of r=0.25. The mesh-width is $(\frac{2}{128}, \frac{1}{64}, \frac{2}{128})$. For the parameters $(Ca, Re) = (0.25, 1.5)$, $(0.2, 4)$ (top row) the flow field inside the droplet has a single vortex, whereas for $(Ca, Re) = (0.15, 10)$, $(0.1, 20)$ (bottom row) we find two vortices.

of surface tension and its discretization on the overall convergence behavior and the improvement of mass conservation properties.

Our scheme employs a standard staggered grid finite difference discretization and a projection method with a fifth-order WENO scheme. The free surface between the two fluid phases is tracked with a LS approach. Here, the interface conditions are implicitly incorporated into the momentum equations by the CSF method and surface tension is evaluated using a smoothed delta functional and an appropriate third-order interpolation scheme. Altogether, our approach exhibits a second-order convergence away from the interface and a first-order convergence near the interface

DOI: 10.1002/fld

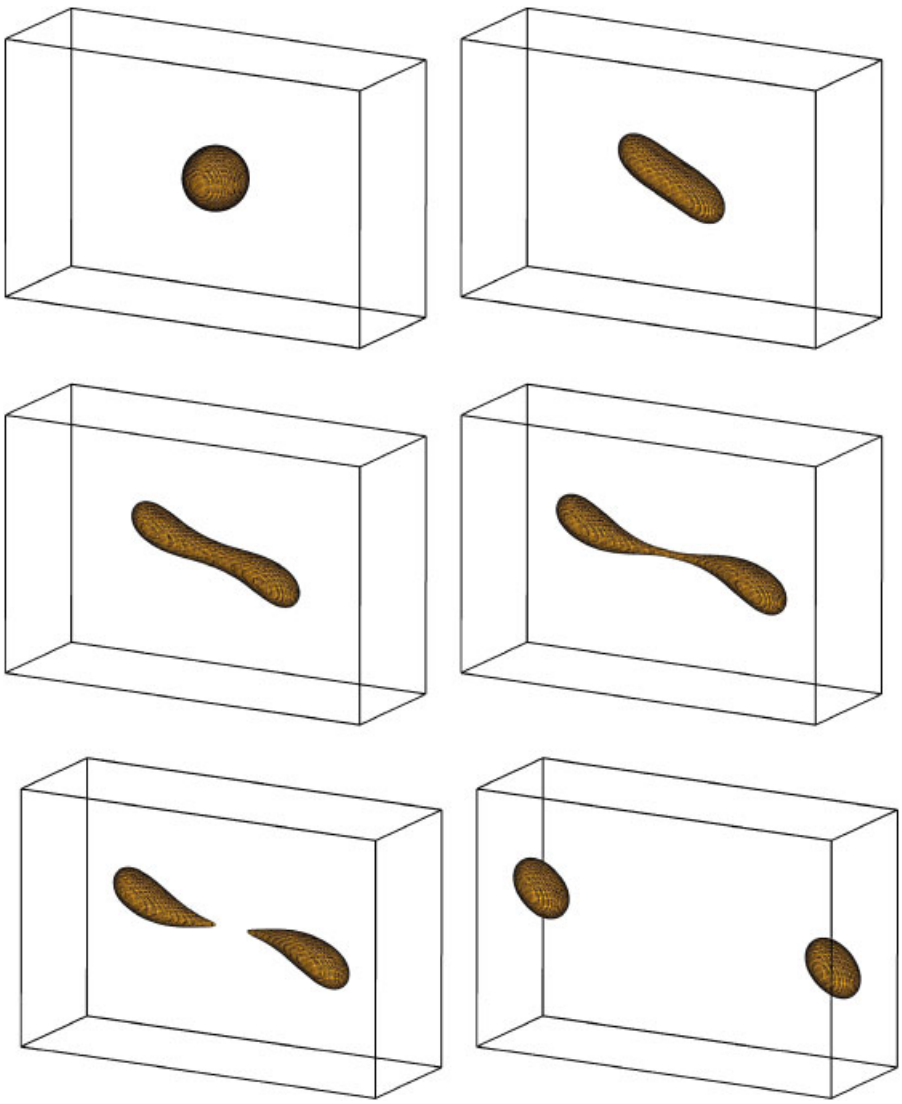

Figure 13. Instationary results obtained for the parameter setting $(Ca, Re) = (0.15, 15)$. Depicted are the configurations of the free surface at the dimensionless times $t^* = 0$, $t^* = 334.8$, $t^* = 379.2$, $t^* = 396.0$, $t^* = 397.2$, $t^* = 416.40$ (upper left to lower right). The simulation domain is $3 \times 1 \times 2$ and the droplet has a radius of $r = 0.25$. The mesh-width is $(\frac{3}{192}, \frac{1}{64}, \frac{2}{128})$.

if the smoothed delta functional is employed; i.e. in the presence of surface tension force. To cope with the unsatisfactory conservation properties of the LS approach, we employ an improved reinitialization procedure combined with a global fixed point iteration. The results of our numerical experiments clearly show this anticipated convergence behavior. Furthermore, the presented results obtained for the rising air bubble clearly show that the employment of a numerical scheme ensuring mass conservation with a higher transport scheme is necessary to obtain high-quality results in

DOI: 10.1002/fld

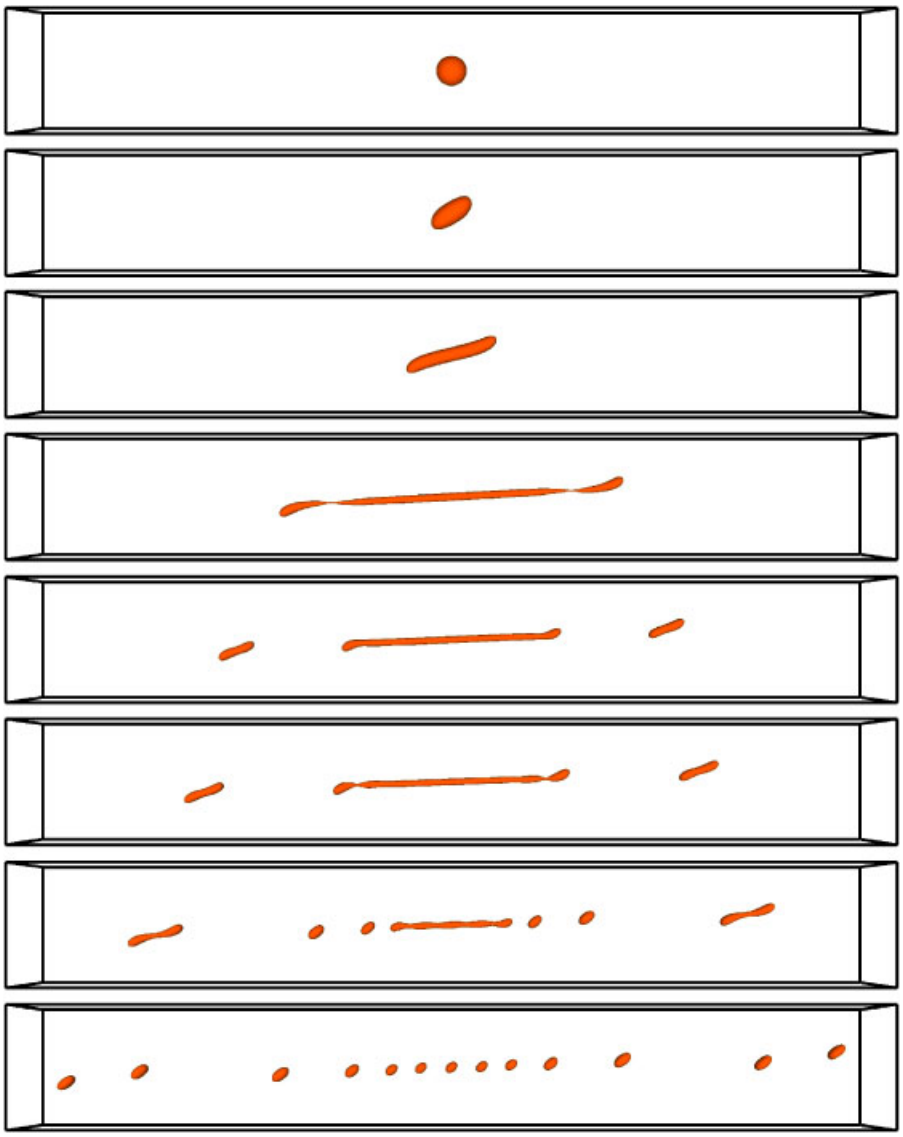

Figure 14. Instationary results obtained for the parameter setting $(Ca, Re) = (0.1, 25)$. Depicted are the configurations of the free surface at the dimensionless times $t^* = 0$, $t^* = 178.8$, $t^* = 238.8$, $t^* = 330.0$, $t^* = 358.8$, $t^* = 373.2$, $t^* = 394.8$, $t^* = 418.8$ (top to bottom). The simulation domain is $14 \times 1 \times 2$ and the droplet has a radius of $r = 0.25$. The mesh-width is $(\frac{14}{896}, \frac{1}{64}, \frac{2}{128})$.

long-time simulations. Moreover, our study indicates that the simulation of bubble dynamics requires a three-dimensional simulation to capture the true physical deformation and behavior. Finally, we considered the deformation of a droplet in shear flow with moderate Reynolds numbers and the presented results correspond very well to those obtained by VOF schemes and the experimental data of [16].

DOI: 10.1002/fld

ACKNOWLEDGEMENTS

This work was supported by the Sonderforschungsbereich 611 *Singular phenomena and scaling in mathematical models* funded by the *Deutsche Forschungsgemeinschaft*.

REFERENCES

1. Lefebvre A. *Atomization and Sprays*. Taylor & Francis: London, 1989.
2. Harlow F, Welch J. Numerical calculation of time-dependent viscous incompressible flow of fluid with free surface. *The Physics of Fluids* 1965; **8**:2182–2189.
3. Daly BJ. Numerical study of two fluid Rayleigh–Taylor instability. *The Physics of Fluids* 1967; **10**:297–307.
4. Daly BJ. Numerical study of the effect of surface tension on interface instability. *The Physics of Fluids* 1969; **12**:1340–1354.
5. Amsden A, Harlow F. A simplified MAC technique for incompressible fluid flow calculations. *Journal of Computational Physics* 1970; **6**:322.
6. Griebel M, Dornseifer T, Neunhoeffer T. *Numerical Simulation in Fluid Dynamics*, *A Practical Introduction*. SIAM: Philadelphia, 1998.
7. Griebel M, Neunhoeffer T, Regler H. Algebraic multigrid methods for the solution of the Navier–Stokes equations in complicated domains. *International Journal of Numerical Methods for Heat and Fluid Flow* 1998; **26**:281–301.
8. Neunhoeffer T. Numerische simulation von Erstarrungsprozessen unterkühlter Flüssigkeiten unter Berücksichtigung von Dichteunterschieden. *Dissertation*, Fakultät für Informatik der Technischen Universität München, 1997.
9. Tryggvason G, Bunner B, Esmaeeli A, Juric D, Al-Rawahi N, Tauber W, Han J, Nas S, Jan YJ. A front tracking method for the computations of multiphase flow. *Journal of Computational Physics* 2001; **169**:708–759.
10. Unverdi S, Tryggvason G. A front-tracking method for viscous, incompressible multi-fluids flow. *Journal of Computational Physics* 1992; **100**:25–37.
11. DeBar R. Fundamentals of the KRAKEN code. *Report ucir-760*, Lawrence Livermore National Laboratory, 1974.
12. Noh W, Woodward P. SLIC—simple line interface calculation. In *Fifth International Conference on Fluid Dynamics*, Vooren AV, Zandbergen P (eds). Lecture Notes in Physics, vol. 59. Springer: Berlin, 1976; 330–340.
13. Hirt CW, Nichols BD. Volume of fluid VOF method for the dynamics of free boundaries. *Journal of Computational Physics* 1981; **39**:201–225.
14. Lafaurie B, Nardone C, Scardovelli R, Zaleski S, Zanetti G. Modelling merging and fragmentation in multiphase flows with SURFER. *Journal of Computational Physics* 1994; **113**:134–147.
15. Gueyffier D, Li J, Nadim A, Scardovelli R, Zaleski S. Volume-of-fluid interface tracking with smoothed surface stress methods for three-dimensional flows. *Journal of Computational Physics* 1999; **152**:423–456.
16. Li J, Renardy YY, Renardy M. Numerical simulation of breakup of a viscous drop in simple shear flow through a volume-of-fluid method. *Physics of Fluids* 2000; **12**:269–282.
17. Li J, Renardy YY. Numerical study of flows of two immiscible liquids at low Reynolds number. *SIAM Review* 2000; **42**:417–439.
18. Béliveau A, Fortin A, Demay Y. A two-dimensional numerical method for the deformation of drops with surface tension. *International Journal of Computational Fluid Dynamics* 1998; **10**:225–240.
19. Ginzburg I, Wittum G. Two-phase flows on interface refined grids modeled with VOF, staggered finite volumes, and spline interpolants. *Journal of Computational Physics* 2001; **166**:302–335.
20. Ginzburg I, Wittum G, Zaleski S. Adaptive multigrid computations of multiphase flows. In *Numerical Flow Simulation III*, Hirschel EH (ed.). Notes on Numerical Fluid Mechanics and Multidisciplinary Design, vol. 82. Springer: Berlin, 2002; 77–96.
21. Osher S, Sethian J. Fronts propagating with curvature-dependent speed: algorithms based on Hamilton–Jacobi formulations. *Journal of Computational Physics* 1988; **79**:12–49.
22. Sethian JA. *Level Set Methods and Fast Marching Methods*. Cambridge University Press: Cambridge, 1999.
23. Osher S, Fedkiw R. *Level Set Methods and Dynamic Implicit Surfaces*. Applied Mathematical Sciences, vol. 153. Springer: New York, Berlin, Heidelberg, 2003.
24. Adalsteinsson D, Sethian JA. A fast level set method for propagating interfaces. *Journal of Computational Physics* 1995; **118**:269–277.
25. Chopp DL. Computing minimal surfaces via level set curvature flow. *Journal of Computational Physics* 1993; **106**:77–91.

DOI: 10.1002/fld

26. Chen S, Merriman B, Osher S, Smereka P. A simple level set method for solving Stefan problems. *Journal of Computational Physics* 1997; **135**:8–29.
27. Merriman B, Bence J, Osher S. Motion of multiple junctions: a level set approach. *Journal of Computational Physics* 1994; **122**:334–363.
28. Sussman M, Smereka P, Osher S. A level set approach for computing solutions to incompressible two-phase flow. *Journal of Computational Physics* 1994; **114**:146–159.
29. Sussman M, Fatemi E. An efficient, interface preserving level set re-distancing algorithm and its application to incompressible fluid flow. *SIAM Journal on Scientific Computing* 1999; **20**:1165–1191.
30. Russo G, Smereka P. A remark on computing distance functions. *Journal of Computational Physics* 2003; **163**:51–67.
31. Enright D, Fedkiw R, Ferziger J, Mitchell I. A hybrid particle level set method for improved interface capturing. *Journal of Computational Physics* 2002; **183**:83–116.
32. Peng D, Merriman B, Osher S, Zhao H, Kang M. A PDE-based fast local level set method. *Journal of Computational Physics* 1999; **155**:410–438.
33. Bänsch E. Finite element discretization of the Navier–Stokes equations with a free capillary surface. *Technical Report*, Universität Bremen, 1999.
34. Dziuk G. Finite elements for the Beltrami operator on arbitrary surfaces. *Partial Differential Equations and Calculus of Variations*, vol. 1357. Springer: Berlin, 1988; 142–155.
35. Dziuk G. An algorithm for evolutionary surfaces. *Numerische Mathematik* 1991; **58**:603–611.
36. Ho LW, Patera AT. A Legendre spectral element method for simulation of unsteady incompressible viscous free-surface flows. *Computer Methods in Applied Mechanics and Engineering* 1990; **80**:355–366.
37. Ho LW, Rønquist EM. Spectral element solution of steady incompressible viscous free-surface flows. *Finite Elements in Analysis and Design* 1994; **16**:207–227.
38. Brackbill JU, Kothe DB, Zemach C. A continuum method for modeling surface tension. *Journal of Computational Physics* 1992; **100**:335–354.
39. van der Pijl SP, Segal A, Vuik C, Wesseling P. A mass conserving level-set method for modelling of multiphase flows. *International Journal for Numerical Methods in Fluids* 2005; **47**:339–361.
40. Kang M, Fedkiw RP, Liu X-D. A boundary condition capturing method for multiphase incompressible flow. *Journal on Scientific Computing* 2000; **15**:323–360.
41. Landau LD, Lifshitz EM. *Fluid Mechanics*. Pergamon Press: Oxford, 1959.
42. Renardy Y, Renardy M. Prost: a parabolic reconstruction of surface tension for the volume-of-fluid method. *Journal of Computational Physics* 2002; **183**:400–421.
43. Francois MM, Cummins SJ, Dendy ED, Kothe DB, Sicilian M, Williams MW. A balanced-force algorithm for continuous and sharp interfacial surface tension models within a volume tracking framework. *Journal of Computational Physics* 2006; **213**:141–173.
44. Kothe DB. Perspectives on Eulerian finite volume methods for incompressible interfacial flows. In *Free Surface Flows*, Kuhlmann HC, Rath H-J (eds). Springer: Berlin, 1999; 267–331.
45. Prosperetti A. Navier–Stokes numerical algorithms for free-surface flow computations: an overview. In *Drop Surface Interactions*, Rein M (ed.). Springer: Berlin, 2002; 237–257.
46. Chang YC, Hou TY, Merriman B, Osher S. A level set formulation of Eulerian interface capturing methods for incompressible fluid flows. *Journal of Computational Physics* 1996; **124**:449–464.
47. Chorin AJ. Numerical solution of the Navier–Stokes equations. *Mathematical Computation* 1968; **22**:745–762.
48. Brown DL, Cortez R, Minion ML. Accurate projection methods for the incompressible Navier–Stokes equations. *Journal of Computational Physics* 2001; **168**:464–499.
49. Jiang GS, Peng D. Weighted ENO schemes for Hamilton–Jacobi equations. *SIAM Journal on Scientific Computing* 2000; **21**:2126–2143.
50. Jiang GS, Shu CW. Efficient implementation of weighted ENO schemes. *Journal of Computational Physics* 1996; **126**:202–228.
51. Shu CW, Osher S. Efficient implementation of essentially non-oscillatory shock-capturing schemes. *Journal of Computational Physics* 1988; **77**:439–471.
52. Croce R, Griebel M, Schweitzer MA. A parallel level-set approach for two-phase flow problems with surface tension in three space dimensions. *Preprint 157*, *Sonderforschungsbereich 611*, Universität Bonn, 2004.
53. Harvie DJE, Davidson MR, Rudman M. An analysis of parasitic current generation in volume of fluid simulations. *Applied Mathematical Modelling* 2006; **30**:1056–1066.

DOI: 10.1002/fld

54. Harvie DJE, Rudman M, Davidson MR. Parasitic current generation in combined level set and volume of fluid immiscible fluid simulations. *Computational Techniques and Applications Conference 2006*, James Cook University, Townsville, Australia, 2008.
55. Engqist B, Tornberg A-K, Tsai R. Discretization of Dirac delta functions in level set methods. *Journal of Computational Physics* 2005; **207**:28–51.
56. Griebel M, Metsch B, Oeltz D, Schweitzer MA. Coarse grid classification: a parallel coarsening scheme for algebraic multigrid methods. *Numerical Linear Algebra with Applications* 2006; **13**:193–214.

DOI: 10.1002/fld